Active control of a turbulent boundary layer based on local surface perturbation

H. L. Bai[1], Y. Zhou[1,†], W. G. Zhang[2], S. J. Xu[3], Y. Wang[1] and R. A. Antonia[4]

[1]Institute for Turbulence–Noise–Vibration Interaction and Control, Shenzhen Graduate School, Harbin Institute of Technology, Shenzhen, China

[2]State Key Laboratory of Aerodynamics, Mianyang 621000, China

[3]School of Aerospace, Tsinghua University, Beijing 100084, China

[4]School of Engineering, University of Newcastle, Callaghan, NSW 2308, Australia

Active control of a turbulent boundary layer has been experimentally investigated with a view to reducing the skin-friction drag and gaining some insight into the mechanism that leads to drag reduction. A spanwise-aligned array of piezo-ceramic actuators was employed to generate a transverse travelling wave along the wall surface, with a specified phase shift between adjacent actuators. Local skin-friction drag exhibits a strong dependence on control parameters, including the wavelength, amplitude and frequency of the oscillation. A maximum drag reduction of 50 % has been achieved at 17 wall units downstream of the actuators. The near-wall flow structure under control, measured using smoke–wire flow visualization, hot-wire and particle image velocimetry techniques, is compared with that without control. The data have been carefully analysed using techniques such as streak detection, power spectra and conditional averaging based on the variable-interval time-average detection. All the results point to a pronounced change in the organization of the perturbed boundary layer. It is proposed that the actuation-induced wave generates a layer of highly regularized streamwise vortices, which acts as a barrier between the large-scale coherent structures and the wall, thus interfering with the turbulence production cycle and contributing partially to the drag reduction. Associated with the generation of regularized vortices is a significant increase, in the near-wall region, of the mean energy dissipation rate, as inferred from a substantial decrease in the Taylor microscale. This increase also contributes to the drag reduction. The scaling of the drag reduction is also examined empirically, providing valuable insight into the active control of drag reduction.

Key words: active control, boundary layer control, boundary layers

1. Introduction

Turbulence control is a field in fluid mechanics where flow is manipulated in order to improve the efficiency of thermo-fluid systems, for example, by reducing

† Email address for correspondence: zhouyu@hitsz.edu.cn

skin-friction drag, or enhancing heat transfer and flow mixing (Liepmann & Narashima 1988). For the purpose of reducing skin-friction drag, passive control techniques such as riblets (e.g. Wash 1983) have achieved limited success. Active control methods have been extensively investigated, including boundary-layer suction or wall heating for delaying transition, modifying fluid viscosity by injection of polymers or changing fluid temperature, using compliant walls, suction and blowing, spanwise wall oscillation, and transverse travelling waves. See Gad-el-Hak (2000), Karniadakis & Choi (2003), Kim (2003) and Kasagi, Suzuki & Fukagata (2009) for recent reviews.

Past experimental and numerical studies indicate a close association between quasi-streamwise vortices (referred to as streamwise vortices hereinafter for simplicity) and large wall shear stress. The production of mean Reynolds stress (subsequently viscous drag) is linked directly to the dynamics of streamwise vortices in the wall region (Bernard, Thomas & Handler 1993). Streamwise vortices are generally located immediately above and displaced laterally from regions of high skin-friction drag (Kravchenko, Choi & Moin 1993; Orlandi & Jiménez 1994). The well-known events, i.e. sweeps and ejections, bursts and streak-like structures, are all related to streamwise vortices (e.g. Kim 1983). Both ejections and sweeps are induced by the vortices. The ejection process involves slow-moving fluid being lifted up from the wall on the updraught side of the vortices, resulting in the formation of a low-speed streak. The lifted slow-moving fluid induces an inflection in the mean velocity profile. When intensified, the inflection results in a secondary instability and a subsequent burst of Reynolds stress, which transfers energy from large to small scales, and produces turbulent fluctuations. The ejection is the central mechanism for energy, momentum and vorticity transfer between the inner and outer layers (e.g. Kline *et al.* 1967). On the other hand, the sweep on the downdraught side of the vortices produces a high-speed streak and is responsible for an increase in wall friction (Kravchenko *et al.* 1993; Orlandi & Jiménez 1994). It is therefore particularly important in the context of drag reduction. The two events account for approximately 80 % of the turbulent energy production (Lu & Willmarth 1973).

Locally controlling individual streamwise vortices in the near-wall region is the key to drag reduction techniques. Occurring within 15 wall units from the wall (Wallace, Eckelmann & Brodkey 1972), sweeps and ejections are closely connected in the bursting process. Manipulating the near-wall region will directly influence ejections and subsequently sweeps. Therefore, it is feasible to implement wall-based control schemes, e.g. riblets, spanwise wall oscillations, compliant walls, suction and blowing, and transverse travelling waves, for reduction of skin-friction drag. Applying an open-loop-controlled oscillating spanwise Lorentz force to a channel flow, Berger *et al.* (2000) found that skin-friction drag could be reduced by 40 %, though this control scheme was impracticable because of a very low efficiency. A spanwise oscillating wall could reduce the skin-friction drag up to 45 % (Choi, DeBisschop & Clayton 1998), but the maximum net energy saving is only 7 % due to the auxiliary mechanical movement (Quadrio & Ricco 2004). Du & Karniadakis (2000) and Du, Symeonidis & Karniadakis (2002) investigated using direct numerical simulation (DNS) the effectiveness of a transverse travelling wave, induced by a near-wall spanwise force, on drag reduction. They reported a drag reduction exceeding 50 % and observed significant modification to near-wall streaks. Their preliminary experiments with Lorentz actuators and shape-memory alloys produced results consistent with the DNS data. Nevertheless, this technique has yet to be demonstrated experimentally (Karniadakis & Choi 2003).

Wall deformation is considered to be one of the most promising candidates among various actuators because of its robustness against hostile environments

(Endo, Kasagi & Suzuki 2000). For example, Grosjean *et al.* (1998) showed that pneumatic wall-deformation actuators based on micro-electromechanical system (MEMS) techniques survived transonic flight tests with large temperature variations. Wilkinson & Balasubramanian (1985) and Kang & Choi (2000) demonstrated that the streaky structures in a turbulent boundary layer (TBL) could be altered by means of selective wall deformation. Segawa *et al.* (2002) devised an actuator array to create wall-normal oscillation and decreased the regularity of streaky structures. However, the drag reduction was not reported. In their boundary-layer control investigation, Itoh *et al.* (2006) used a loudspeaker to excite a flexible polythene sheet of 5000×5000 wall units, flush with a flat wall surface, to form a transverse travelling wave, achieving only 7.5 % drag reduction. A question that emerges from these previous studies is whether a wall-normal oscillation, if coupled with the travelling wave technique, can produce an even larger drag reduction than with only the travelling wave.

The present work aims at investigating experimentally the reduction of skin-friction drag in a TBL using a spanwise-aligned piezo-ceramic (PZT) actuator array, consisting of 16 or 12 elements. By specifying a phase shift between adjacent actuators, the actuator array can generate a transverse travelling wave along the wall. The control parameters, including the wavelength, amplitude and frequency of the oscillation, and their influence on the skin-friction drag, are investigated. The near-wall flow structure under control is measured using smoke–wire flow visualization, particle image velocimetry (PIV) and hot-wire techniques and compared to that without control. Experimental details are given in § 2. Results are presented and discussed in detail in §§ 3–6. Conclusions are given in § 7.

2. Experimental details

2.1. *Experimental set-up*

Experiments were conducted in a closed-circuit wind tunnel, built by Professor Yu Zhou at The Hong Kong Polytechnic University. The tunnel has a 2.4 m long test section of 0.6 m × 0.6 m. See Huang, Zhou & Zhou (2006) for more details of this tunnel. As shown in figure 1, the boundary layer was produced by a Perspex flat plate, which is supported by four cylindrical struts and placed horizontally in the test section of the tunnel. The plate is 9 mm thick, 2.2 m long and 0.6 m wide, with the leading edge rounded into an elliptic profile (long to short axis = 4:1). The separation between the plate and the ceiling of the test section is 0.45 m. The plate is slightly inclined to ensure a zero pressure gradient along the test section. A 0.2 m long end-flap plate, inclined by approximately 10°, was used to adjust the front stagnation line so as to avoid flow separation at the leading edge of the plate. Following Rebbeck & Choi (2006), two spanwise-aligned arrays of M4 screws, separated longitudinally by 15 mm, were placed at 0.1 m downstream of the leading edge to trip the boundary layer. Each array consisted of a total of 59 screws, each 5 mm above the plate and separated from its adjacent ones by 10 mm. The two arrays of screws were alternately arranged longitudinally. Measurements were mostly performed at a free-stream velocity (U_∞) of 2.4 m s^{-1}, monitored near the exit of the contraction section using a Pitot static tube and a micro-manometer (FCO510, Furness). The micro-manometer has a reading accuracy of 0.25 % and the experimental uncertainty in U_∞ is within ±2 %. The free-stream turbulence intensity is 0.7 % in the presence of the plate. One array of PZT actuators was placed at 1.5 m downstream of the leading edge of the plate. Table 1 shows, given $U_\infty = 2.4$
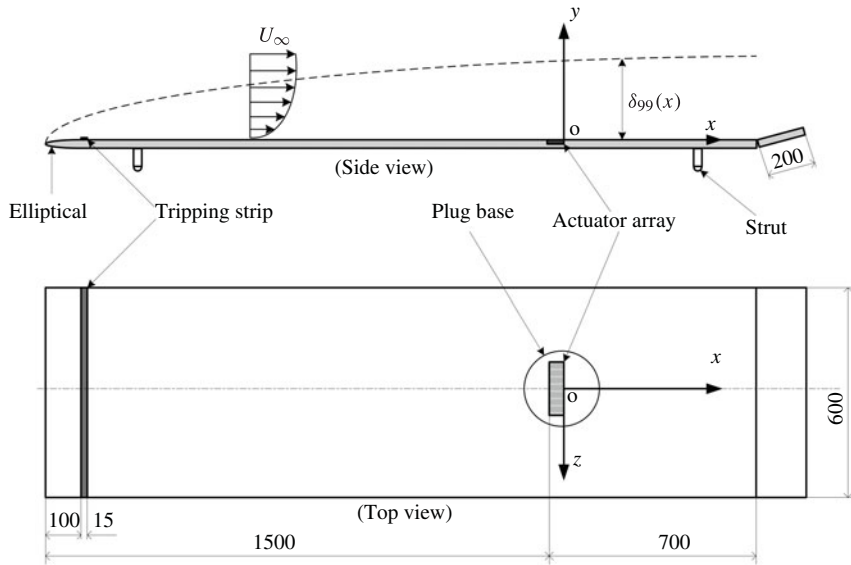
FIGURE 1. Schematic of experimental set-up for the generation of the TBL (not to scale; dimensions in millimetres).

U_∞ (m s^{-1})	δ_{99} (mm)	θ (mm)	Re_θ	H_{12}	u_τ (m s^{-1})
2.4	60	6.5	1000	1.4	0.111
4.0	54	5.8	1540	1.4	0.176

TABLE 1. Characteristic parameters of the uncontrolled TBL.

and 4.0 m s^{-1}, the characteristic parameters of the natural boundary layer at this position, including boundary-layer thickness δ_{99}, momentum thickness θ, shape factor H_{12}, friction velocity u_τ ($\equiv \sqrt{\overline{\tau_w}/\rho}$, where τ_w is local wall shear stress and ρ is fluid density, and overbar denotes time averaging), and Reynolds number Re_θ based on θ and U_∞. The streamwise mean velocity profiles, measured at $x = 0$ and $z = 0$, ± 50 and ± 100 mm using the hot wire, collapsed perfectly, thus confirming the two-dimensionality of the natural boundary layer.

Figure 2 shows schematically the array of actuators, a total of 16 elements. Each element, flush-mounted with the plate surface, has a dimension of 22 mm $\times$ 2 mm $\times$ 0.33 mm (length $\times$ width $\times$ thickness). The tolerance in width is ± 0.1 mm. The actuators are cantilever-supported, with its inactive part (2 mm long) glued to a substrate, which is embedded in a circular plug base. There is a cavity under each actuator so that the active part (20 mm long) of the actuator can vibrate freely. The actuators are separated spanwise by 1 mm. As such, the entire actuator array spans 45 mm in the spanwise direction, occupying an area of 312 (spanwise) $\times$ 139 (streamwise) wall units. The average spacing between near-wall low-speed streaks is estimated to be 100 and 1000 wall units in the z and x directions, respectively (Kline *et al.* 1967), and these streaks are characterized by a broad range of scales (Robinson 1991). See figure 1 for the definition of the coordinate system (x, y, z). Jacobson & Reynolds (1998) experimentally demonstrated, in a laminar boundary layer (turning

FIGURE 2. (*a*) Layout and installation of the 16 PZT actuators (not to scale; dimensions in millimetres). (*b*) One spanwise wave formed at $\varphi_{i,i+1} = 24°$ ($\lambda_z = 45$ mm or 312 wall units); (*c*) $\varphi_{i,i+1} = 0°$ ($\lambda_z = \infty$).

into a turbulent flow once imposed with steady or unsteady disturbances), that the wall-based actuation suppressed coherent structures, thus reducing skin-friction drag. They suggested the necessity to control a fraction of the near-wall streaks in a TBL and proposed that a control modulus should be of the order of 20 and 200 wall units in the z and x directions, respectively. The present actuation greatly exceeds this modulus in the z direction, while it is of the same order of magnitude longitudinally. The gap between the actuator and the wall edge around it is nominally 0.05 mm (refer to detail B in figure 2*a*), or 0.35 wall units. Each actuator was driven by an individual voltage amplifier and guaranteed to have the same peak-to-peak oscillation amplitude at the tip (A_o) as the others by adjusting its effective or root-mean-square (r.m.s.) driving voltage (V_o) of a sinusoidal wave at each working frequency (f_o) in

a dSpace control system (DS1006), which plays the role of function generator. Here, A_o was measured using a laser vibrometer (Polytech OFV 3001 502). The phase shift $\varphi_{i,i+1}$ $(i = 1, 2, \ldots, 15)$ between adjacent actuators could be set and adjusted on the dSpace control system. A discrete wave may be produced along the wall surface for a given $\varphi_{i,i+1}$. For example, at $\varphi_{i,i+1} = 24°$, the 16 actuators form one discrete transverse sinusoidal wave with a wavelength (λ_z) of 45 mm (or 312 wall units) (figure 2b) and, at $\varphi_{i,i+1} = 0°$, oscillate in phase, with a wave of nominal $\lambda_z = \infty$ (figure 2c). The arrangement of the 16 actuators is symmetric about the xy plane at $z = 0$. Instantaneous velocities along the x, y and z axes are designated as U $(= \overline{U} + u)$, V $(= \overline{V} + v)$ and W $(= \overline{W} + w)$, respectively, where u, v and w are the corresponding fluctuating components.

2.2. *Hot-wire, PIV and flow visualization measurements*

A miniature single-wire probe (55P15, Dantec), operated on a constant-temperature anemometer (CTA, Dantec Streamline), was used to measure U in the boundary layer and hence $\overline{U}$. The sensing element is a tungsten wire of 5 µm diameter and approximately 1 mm length, and was calibrated in the free stream using a Pitot static tube. The hot-wire probe was mounted on a computer-controlled three-dimensional (3D) traversing mechanism, whose resolution in the y direction is 10 µm and minimum increment is 50 µm. An overheat ratio of 1.8 was used. The signal from the wire was offset, low-pass-filtered at a cutoff frequency of 1.0 kHz, and then sampled at a frequency of 2.5 kHz using a 16-bit analogue-to-digital converter. The sampling duration for each record is 40 s, long enough to ensure that the r.m.s. value, u_{rms}, of u is converged, within 1 % uncertainty.

A Dantec PIV2100 system was deployed to measure the boundary layer in the xz and yz planes. The flow was seeded with smoke generated from paraffin oil by a smoke generator. The averaged seeding particle diameter is approximately 1 µm. Flow illumination was provided by light sheets, around 0.8 mm thick, produced by two Newwave standard pulse laser sources of a 532 nm wavelength, each with a maximum energy output of 120 mJ pulse^{-1}. The laser pulse lasted for 10 ns. Particle images were captured using one charge-coupled device (CCD) camera (double frames, 2048 pixels $\times$ 2048 pixels). Synchronization between image taking and flow illumination was provided by a Dantec FlowMap Processor (PIV2001 type). The wall surface, actuator array substrate and the plug base were all painted black to minimize background noise. The middle 12 elements of the actuator array were operated during PIV measurements. Measurements in the xz plane were conducted at $y^+ = 5.5$, in the viscous sublayer. Unless otherwise stated, superscript '+' denotes normalization by u_τ measured in the absence of control and/or the kinematic viscosity υ of the fluid. The PIV image covers an area of $x^+ = 0$–306 and $z^+ = \pm153$. The image magnification is 0.021 mm pixel^{-1}. The interval between two successive pulses is 80–100 µs, which was determined *in situ* and corresponded to the fewest pitfalls of velocity vectors. Given a convective velocity $\overline{U}_c^+ = 12$ near the wall (Johansson, Alfredsson & Kim 1991), seeding particles could travel a distance of 0.13 mm, approximately 1 wall unit, for this time interval. Some scattered spot disturbances from the wall surface, possibly due to imperfect painting or dust deposit, may contaminate raw particle images, particularly in the measurements of the xz plane at $y^+ = 5.5$. These disturbances characterized by fixed positions were removed by comparing all the images with each other. A threshold in grey scale was set at 25 % of the full range for the background noise removal. The pixel value was assigned to be unity, when

exceeding the threshold, or zero otherwise, thus producing the filtered image, which contained only the detected spot disturbances. This image was used to refine the raw images. Depardon *et al.* (2005) proposed a method to reduce the optical disturbances from the wall surface in the near-wall PIV measurement. A reference image with the mean pixel value was produced and then subtracted from raw images. Their method could remove most of the disturbances, but not all. In contrast, the present method may identify and remove all the possible spot disturbances. Measurements in the yz plane were conducted at $x^+ = 35$. This plane was normal to the flow. The thickness of the laser light sheet was increased to 1.5 mm in order to capture more valid particles in the PIV images. A mirror of 40 mm $\times$ 40 mm was placed at $x = 300$ mm, with an angle of $45°$ with respect to the yz plane to allow the CCD camera, placed outside the tunnel, to capture the image in the yz plane. The mirror interference to the flow concerned is negligible (Huang *et al.* 2006). The captured image covers an area of $z^+ = -156.5$ to $+156.5$ and $y^+ = 0$–313. The image magnification factor is 0.022 mm pixel^{-1} and the interval between two successive pulses is 80 μs. Spatial cross-correlation, with an interrogation window of 64 pixels $\times$ 64 pixels and a 50 % overlap along the two directions, was calculated to determine velocity vectors, a total of 3969 (63 $\times$ 63). The same number of vorticity data was obtained. Over 2000 pairs of images were taken in each plane. The mean velocity, Reynolds stresses and vorticity all converge to no more than 1 % uncertainty.

The smoke–wire flow visualization was performed in the xz plane to complement the PIV measurements. A nickel–chromium wire of 0.1 mm diameter, strained and supported on a fork attached to the 3D traversing mechanism, was placed at $y^+ = 8$, normalized based on the wall variables at $U_\infty = 2.4$ m s^{-1}, parallel to the wall surface and normal to the flow direction. The wire was painted with high-temperature-resistant paint for a length of 10 wall units and a paint-free interval of 7 wall units. Once the wire coated with paraffin oil was heated by a direct current with a maximum of 30 mA from a tailor-made circuit, the paraffin oil gathered at the parts coated with paint (lower temperature) and, as a result, only the paint-free intervals (higher temperature) produced smoke filaments. Illumination was provided by a continuous laser light sheet 0.8 mm thick in the xz plane of $y^+ = 10$ ($U_\infty = 2.4$ m s^{-1}). The laser beam, guided through an optical fibre, was emitted from an argon ion laser source with a power of 4 W and swept via a cylindrical lens. A digital video camera was used to record the flow field at a frame rate of 25 frames per second (f.p.s.). Here, U_∞ was reduced to 1.5 m s^{-1} since a higher U_∞ resulted in poor flow visualization results.

2.3. *Skin-friction drag measurement*

Local skin-friction drag was estimated through the averaged wall shear stress $\overline{\tau}_w$, calculated based on the slope of the hot-wire-measured $\overline{U}$ in the viscous sublayer. Strictly, $\overline{U}$ should be measured in the region $y^+ < 2$ since $\overline{U}^+/y^+$ is constant over this region only (e.g. Antonia & Kim 1991). However, the use of a hot wire precludes this approach. Here we have followed the procedure outlined by Choi *et al.* (1998), Khoo, Chew & Teo (2000) and Rathnasingham & Breuer (2003). The accurate positioning of the hot-wire probe is crucial for estimating $\overline{\tau}_w$. To this end, we used one method proposed by Hutchins & Choi (2002) based on the wall effect on heat transfer over a hot wire. Firstly, the hot wire was carefully aligned to be normal to the flow direction, parallel to the wall surface, with the approach angle of the hot-wire probe slightly modified to the wall (cf. figures 5 and 7 in Hutchins & Choi 2002).
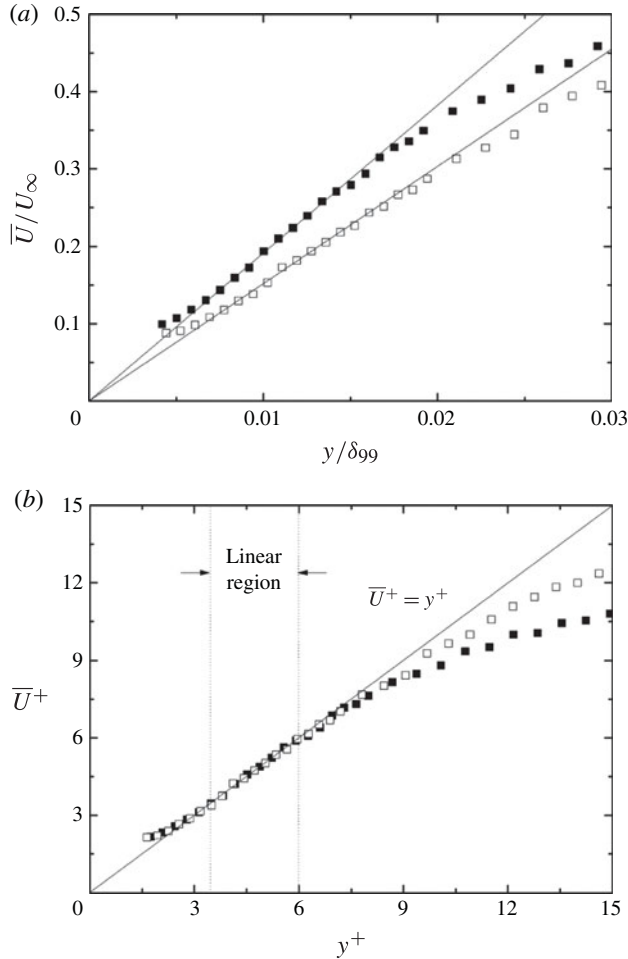
FIGURE 3. Distributions of the mean streamwise velocity (*a*) $\overline{U}/U_\infty$ and (*b*) $\overline{U}^+$ in the near-wall region, measured using a hot wire placed at $x^+ = 35$ and $z^+ = 0$: ■, without control; □, with control ($A_o^+ = 1.66$, $f_o^+ = 0.39$ and $\lambda_z^+ = 416$ (or $\varphi_{i,i+1} = 18°$), $\delta_{\tau_w} = -20\%$). The solid line is the least-squares fit to the measured $\overline{U}/U_\infty$ data over $y/\delta_{99} = 0.006$–0.016.

Secondly, the probe was positioned at an assumed $y = 2$ mm away from the wall and moved vertically towards the wall surface until the online-monitored $\overline{U}$ was observed to increase due to the wall effect on the heat transfer from the wire (Khoo *et al.* 2000; Hutchins & Choi 2002). Thirdly, the linear distribution of $\overline{U}$ with respect to y was least-squares-fitted. The intercept of the fitted line with the y axis, corresponding to $\overline{U} = 0$, was considered to be the wall surface and the new origin of the y axis. Although determined in the absence of control, the origin of the y axis remained unchanged even under control. With five repeated measurements, the standard deviation in estimated $\overline{\tau}_w$ is within $\pm 2\%$.

Figure 3(*a*) illustrates typical $\overline{U}$ distributions measured at $x^+ = 35$ and $z^+ = 0$. The data, with or without control, collapse well with the fitting lines (solid) over the range of $y/\delta_{99} = 0.006$–0.02. Once normalized by actual wall variables, the law of the wall, i.e. $\overline{U}^+ = y^+$, is evident for both uncontrolled and controlled cases (figure 3*b*) over
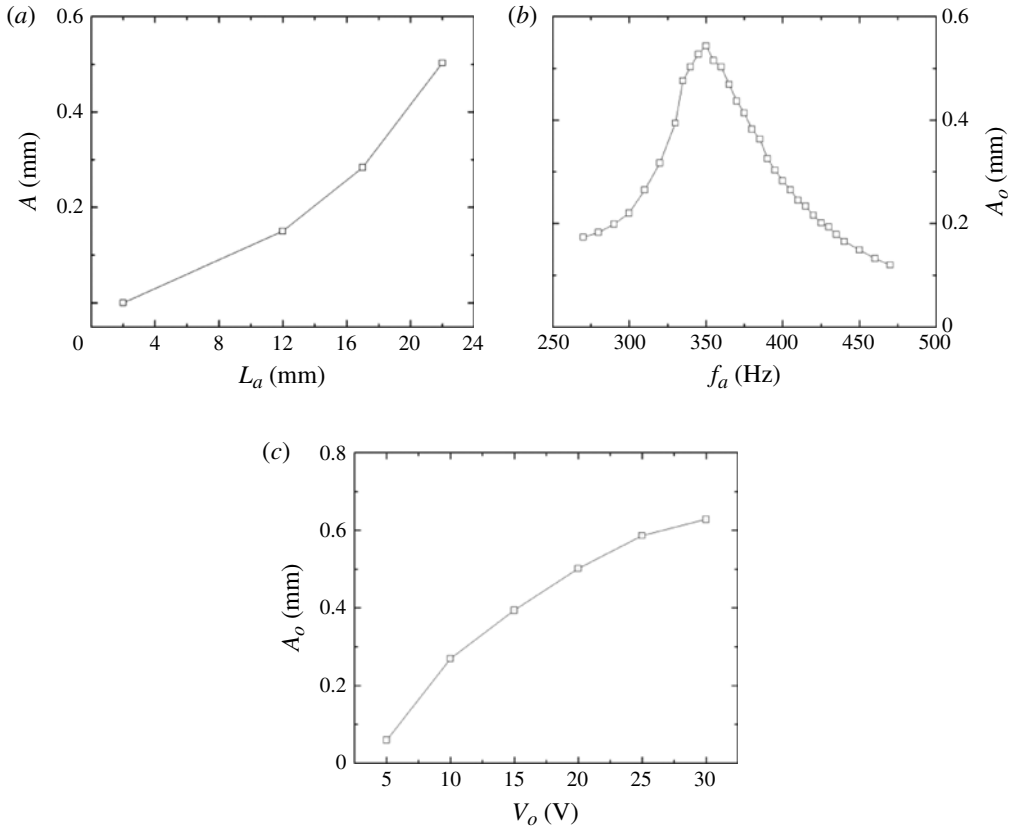
FIGURE 4. (*a*) Typical dependence of the actuator peak-to-peak oscillation amplitude A on the distance L_a from the fixed end (driving voltage $V_o = 20$ V, driving frequency $f_o = 300$ Hz). (*b*) Typical dependence of A at the actuator tip, A_o, on f_o at $V_o = 10$ V. (*c*) Typical dependence of A_o on V_o at $f_o = 300$ Hz. Here $U_\infty = 0$.

$y^+ = 3.5$–6, thus providing a validation for the $\overline{\tau}_w$ estimate. The local skin-friction reduction is defined by

$$\delta_{\tau_w} = \frac{(\overline{\tau}_w)_{on} - (\overline{\tau}_w)_{off}}{(\overline{\tau}_w)_{off}} \times 100\,\%, \tag{2.1}$$

where subscripts *on* and *off* denote measurements with and without control, respectively.

3. Dynamic characteristics and perturbation to flow of a single actuator

Every actuator used was carefully characterized. With the actuator cantilever-supported, its peak-to-peak amplitude of oscillation A depends on the distance L_a from the fixed end, as well as on the frequency of oscillation f_o and r.m.s. voltage V_o. It is apparent that A achieves the maximum A_o at the actuator tip (figure 4*a*). The typical dependence of A_o on f_o, obtained at $V_o = 10$ V, shows a pronounced peak at $f_o \approx 350$ Hz (figure 4*b*) due to the occurrence of the first-mode resonance. This resonance may take place at a frequency between 350 and 400 Hz for other

actuators. At a fixed f_o, A_o increases monotonically with increasing V_o (figure 4c). At $f_o = 300$ Hz and $V_o = 30$ V, A_o exceeds 0.6 mm, approximately 4 wall units, comparable to the viscous-sublayer thickness of a natural TBL.

The perturbation of one single actuator, operated at $f_o^+ = f_o \upsilon / u_\tau^2 = 0.171$ and $A_o^+ = A_o u_\tau / \upsilon = 3.2$, to flow was characterized using a single hot wire moveable in the xy and yz planes at $U_\infty = 4.0$ m s^{-1}. The hot wire was traversed over $y^+ \approx 0$–30 and $z^+ = -25$ to $+25$ in the yz plane of $x^+ = 50$. The measurement interval is $(\Delta y^+, \Delta z^+) = (1, 5)$. The area examined was $x^+ = 50$–350 and $y^+ \approx 0$–30 in the xy plane of $z = 0$, and the measurement interval is $(\Delta x^+, \Delta y^+) = (10, 1)$. Figure 5(a,b) presents the iso-contours of $\Delta \overline{U}^+ = \overline{U}_p^+ - \overline{U}^+$ in the yz or xy plane, where subscript p denotes perturbed flow. The oncoming flow was disturbed largely right above the oscillating actuator, up to $y^+ = 25$ and $x^+ > 350$ downstream. Strong perturbations are evident above the side gaps: one with the maximum $\Delta \overline{U}^+ = -1.2$ residing at about $y^+ = 13$ and $z^+ = 9$, and another with $\Delta \overline{U}^+ = -0.6$ at about $y^+ = 10$ and $z^+ = -8$. A slightly positive $\Delta \overline{U}^+$ occurs near the wall downstream of the actuator tip. The reduced $\overline{U}$ above the actuator indicates the transport of low-momentum fluid away from the wall. The negative-signed disturbance $\Delta \overline{U}^+$ is flanked on both sides by the positive-signed $\Delta \overline{U}^+$, indicating the transport of high-momentum fluid towards the wall. Using a two-component laser Doppler anemometer (LDA), Jacobson & Reynolds (1998) measured the disturbed flow above a single cantilever-supported PZT-actuator with a configuration similar to the present one. Their $\Delta \overline{U}$ above the actuator with equal side gaps (0.05 mm) showed a pattern resembling that in figure 5(a,b), and $\Delta \overline{V}$ was also negative above the actuator but positive over both side gaps, indicating the transport of high-momentum fluid towards the wall. Their fluorescent dye flow visualization displayed one pair of streamwise vortices above the side gaps.

The Δu_{rms}^+ contours, corresponding to $\Delta \overline{U}^+$, in the yz and xy planes are shown in figure 5(c,d), respectively. The maximum Δu_{rms}^+ occurs at $15 < y^+ < 20$, and slightly negative Δu_{rms}^+ is observed in the xy plane. Jacobson & Reynolds (1998) also observed positive Δu_{rms} and Δv_{rms} in this plane aligned with the narrow side gap of the actuator, though their Δu_{rms} and Δv_{rms} were less than 20 %, in magnitude, of $\Delta \overline{U}$ and $\Delta \overline{V}$, respectively. The present Δu_{rms} is no more than 30 % of $\Delta \overline{U}$.

4. Control performance

4.1. *Dependence of drag reduction on control parameters*

The performance of the transverse travelling wave, in terms of δ_{τ_w}, depends on a number of parameters, including A_o^+, f_o^+, λ_z^+ ($= \lambda_z u_\tau / \upsilon$) and $\varphi_{i,i+1}$, where λ_z^+ and $\varphi_{i,i+1}$ are not independent of each other and specifying λ_z^+ gives $\varphi_{i,i+1}$ or vice versa.

4.1.1. *Dependence of δ_{τ_w} on f_o^+ and A_o^+*

Figure 6(a) presents the dependence of δ_{τ_w}, measured at $x^+ = 35$ and $z^+ = 0$, on f_o^+ given $\lambda_z^+ = 416$ ($\varphi_{i,i+1} = 18°$) and $A_o^+ = 1.11$, 1.66, 1.94 and 2.22. At $A_o^+ = 1.11$, δ_{τ_w} declines slowly and insignificantly from $f_o^+ = 0.13$ to 0.32, not more than 5 %. However, the drop is appreciably accelerated for larger f_o^+, and then appears to approach its asymptotic value, approximately -15 %, for f_o^+ greater than a critical frequency, $f_{o,c}^+ = 0.58$. At $A_o^+ \geqslant 1.66$, δ_{τ_w} is apparently more sensitive to f_o^+. With increasing f_o^+, δ_{τ_w} declines, becoming more pronouncedly negative. The decline of δ_{τ_w} is rather rapid up to $f_{o,c}^+ = 0.52$, 0.39 and 0.4 for $A_o^+ = 1.66$, 1.94 and 2.22, respectively, and levels off for a further increase in f_o^+. Control techniques based on a spanwise
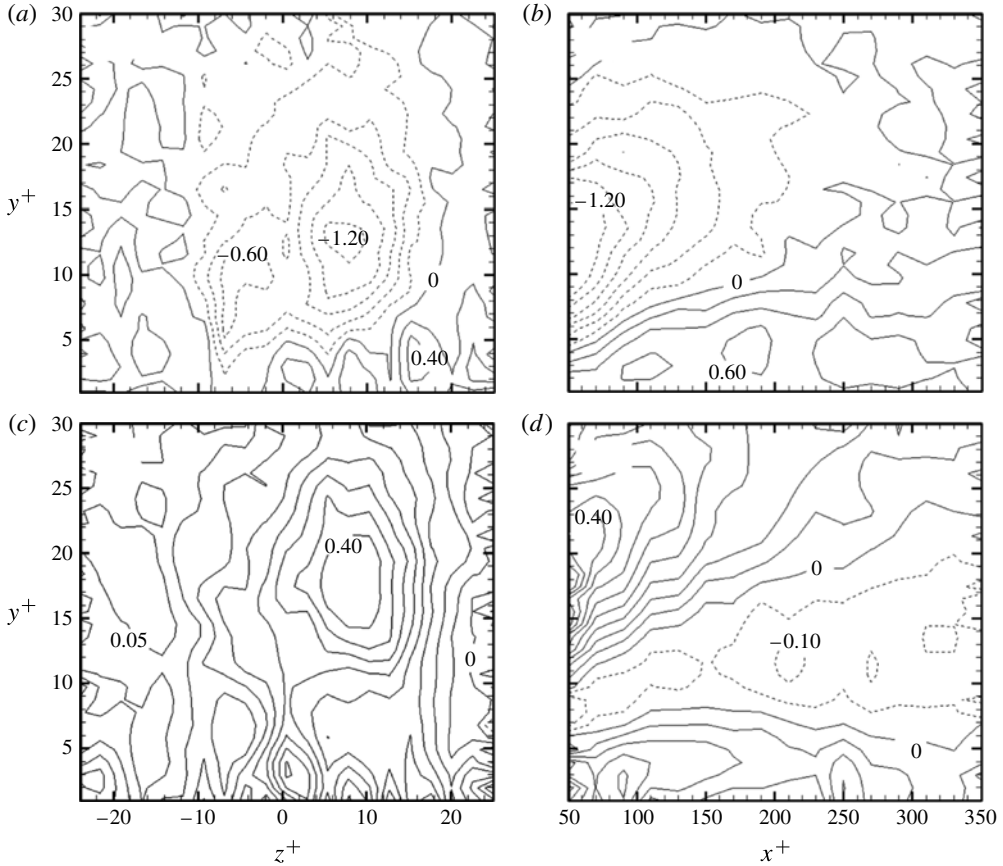
FIGURE 5. Perturbations by one single actuator working at $f_o^+ = 0.171$ and $A_o^+ = 3.2$:
(*a*) iso-contours of $\Delta\overline{U}^+$ in the *yz* plane; (*b*) the *xy* plane, the contour increment $\Delta = 0.2$;
(*c*) iso-contours of the corresponding Δu_{rms}^+ in the *yz* plane; (*d*) the *xy* plane, $\Delta = 0.05$.
The actuator is symmetrical about $z^+ = 0$, with its sides at $z^+ = \pm 10$ and tip at $x^+ = 0$.
Here $U_\infty = 4.0$ m s^{-1}.

oscillatory Lorentz force (Berger *et al.* 2000; Pang & Choi 2004) and a transverse
travelling force wave (Du *et al.* 2002) also displayed a strong dependence of drag
reduction on the excitation frequency. Their excitation frequencies are 0.002–0.04,
0.005–0.02 and 0.01–0.2, respectively. Our discrete actuators are required to work
on higher frequencies to achieve a large reduction in drag. This conforms to Du
et al.'s (2002) suggestion that, owing to the gaps between the discrete positive and
negative actuation regions, the effective wavelength was smaller in the non-ideal wave
compared with the ideal wave, and thus a larger oscillation frequency was needed for
the former in order to suppress the near-wall streaks and to achieve a large reduction
in drag.

Figure 6(*b*) presents the dependence of δ_{τ_w} on A_o^+ ($\lambda_z^+ = 416$ or $\varphi_{i,i+1} = 18°$). The
wall deformation may be considered to be hydraulically smooth because the maximum
A_o^+ is less than 5 wall units (Schlichting & Gersten 2000). Note that perturbation to
flow is produced through actuation-induced flow, rather than the wall displacement
per se (e.g. Jacobson & Reynolds 1998). Two different f_o^+ ($= 0.39$ and 0.65) were
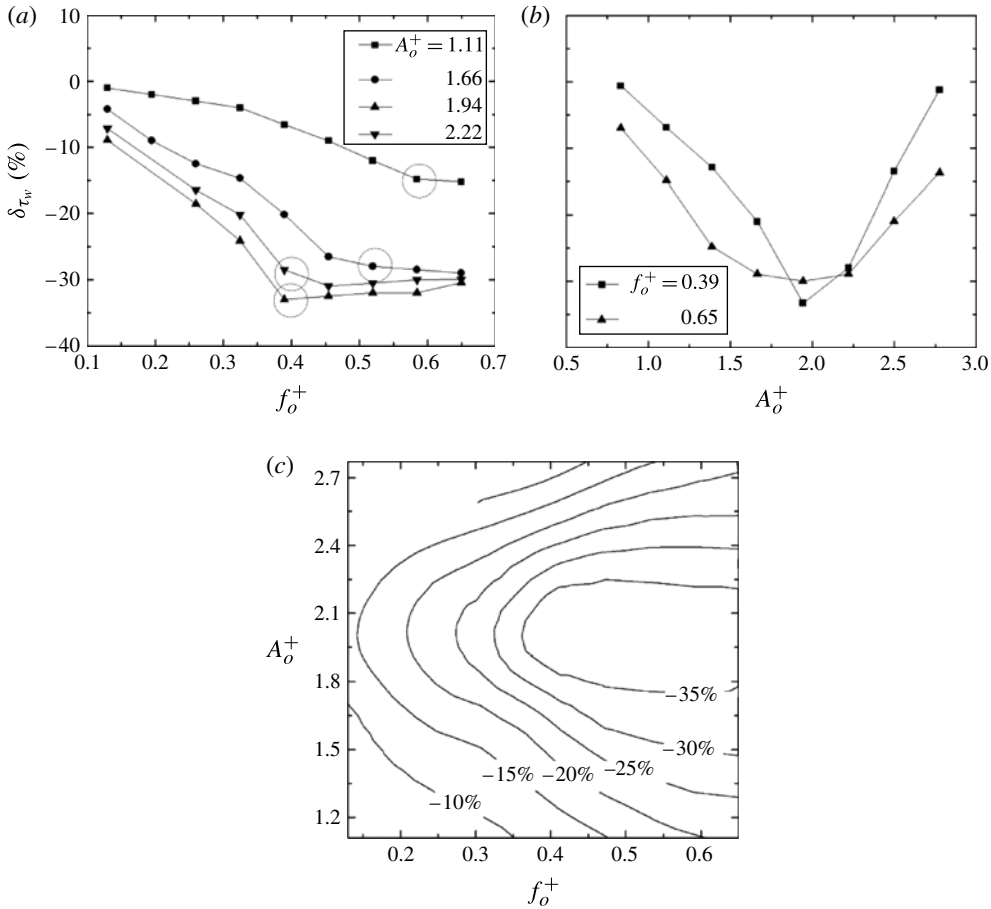
FIGURE 6. Dependence of δ_{τ_w} on (*a*) f_o^+, (*b*) A_o^+ and (*c*) both f_o^+ and A_o^+. The wavelength formed by the actuators is $\lambda_z^+ = 416$ (or $\varphi_{i,i+1} = 18°$). Here $U_\infty = 2.4$ m s^{-1}. The dashed circles in panel (*a*) indicate the points corresponding to the critical frequencies.

examined in the present work. At $A_o^+ = 0.83$, δ_{τ_w} is no more than 10 % for either f_o^+. However, δ_{τ_w} dips rapidly in both cases from $A_o^+ = 0.83$ to 1.94, where δ_{τ_w} reaches the minimum, -30 % for $f_o^+ = 0.65$ or -35 % for $f_o^+ = 0.39$, and climbs quickly for a further increasing A_o^+, especially at the lower f_o^+. The present perturbation to flow is surely well beyond A_o^+. As shown in figure 5, given $A_o^+ = 3.2$, the location of strong flow change ($\Delta \overline{U}^+$), which is an indicator for the penetration depth Λ into the flow, resides mainly at $10 < y^+ = \Lambda^+ < 15$. Then, following a linear interpolation, $A_o^+ \approx 2$ would probably produce a Λ^+ of 6–9. In Du *et al.*'s (2002) DNS study, a spatial transverse travelling wave was formed in terms of a spanwise force that was confined within the viscous sublayer. The force had its maximum on the wall and decayed exponentially away from it. They found that most of the near-wall streaky structures were weakened and even eliminated and the largest drag reduction (more than 50 %) was accordingly achieved when the penetration depth was comparable to the viscous-sublayer thickness. Beyond this depth, however, the skin-friction drag increased.

Iso-contours (figure 6*c*) of δ_{τ_w} in the A_o^+–f_o^+ plane ($\lambda_z^+ = 416$ or $\varphi_{i,i+1} = 18°$) provide a full picture of the dependence of δ_{τ_w} on both A_o^+ and f_o^+. The minimum δ_{τ_w}
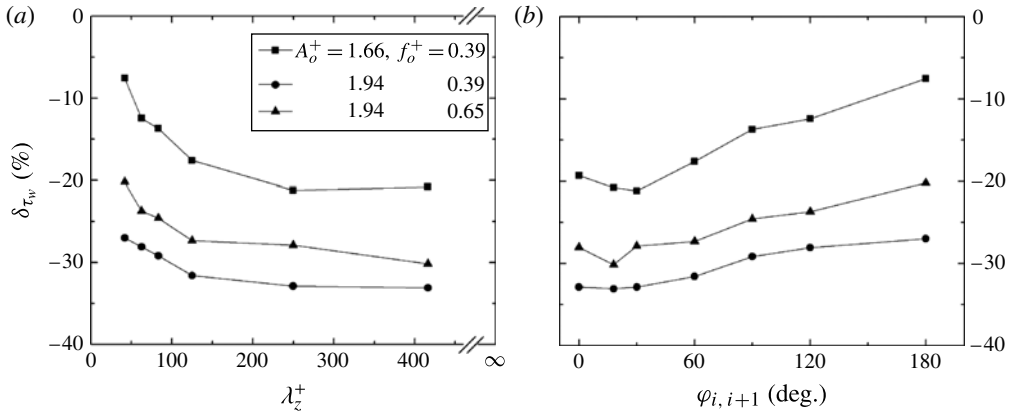
FIGURE 7. Dependence of δ_{τ_w} on (*a*) λ_z^+ and (*b*) $\varphi_{i,i+1}$ at $(A_o^+, f_o^+) = (1.66, 0.39)$, $(1.94, 0.39)$ and $(1.94, 0.65)$. Here $U_\infty = 2.4$ m s^{-1}.

occurs in the region of $f_o^+ \geqslant 0.39$ and $1.8 < A_o^+ < 2.2$. It can be easily demonstrated that the control energy is proportional to $(A_o f_o)^2$ of the travelling wave. It is then found from figure 6(*c*) that more energy input may not necessarily correspond to a larger reduction in drag; rather, there is a band of energy input around $A_o^+ \approx 2$ and $f_o^+ \geqslant 0.39$ where the maximum drag reduction is achieved. Du *et al.* (2002) also noted that the maximum drag reduction was achieved only with the energy input close to a threshold. In the Lorentz force oscillation, Pang & Choi (2004) observed that a region of high drag reduction occurred in the St–T_o^+ plane, where T_o^+ was the normalized oscillation period and St was the Stuart number representing the strength of magnetic force relative to the inertia force of fluid, and the product $St T_o^+$, connected to the energy input, was proportional to the near-wall oscillating flow region enveloped by the Stokes layer resulting from the Lorentz-force oscillation. On another note, in figure 6(*c*), the contours around the region of the minimum δ_{τ_w} at $f_o^+ < 0.47$ are densely separated, relatively to others, implying a relatively strong dependence of δ_{τ_w} on f_o^+ and A_o^+ in view of the identical contour increment in this plot.

4.1.2. *Dependence of δ_{τ_w} on λ_z^+ and $\varphi_{i,i+1}$*

Variation in λ_z^+ is realized by changing $\varphi_{i,i+1}$. Figure 7 presents the dependence of δ_{τ_w} on both λ_z^+ and $\varphi_{i,i+1}$ for $(A_o^+, f_o^+) = (1.66, 0.39)$, $(1.94, 0.39)$ and $(1.94, 0.65)$. Note that $\varphi_{i,i+1} = 0°$ ($\lambda_z^+ = \infty$), $180°$ (42) and $24°$ (312) correspond to the in-phase oscillations, the anti-phase oscillations and that the entire 16 oscillating actuators form one discrete spanwise sinusoidal wave, respectively. The shortest wavelength ($\lambda_z^+ = 42$) is determined by the width of two adjacent actuators with $\varphi_{i,i+1} = 180°$. As shown in figure 7(*a*), δ_{τ_w} is quite appreciable at $\lambda_z^+ = 42$, regardless of the combination of A_o^+ and f_o^+. From $\lambda_z^+ = 42$ to 120, δ_{τ_w} declines quickly. However, beyond $\lambda_z^+ = 120$, δ_{τ_w} drops less rapidly and then asymptotically approaches a constant with $\lambda_z^+ \to \infty$, albeit different for different (A_o^+, f_o^+) combinations. The minimum δ_{τ_w} occurs at $\lambda_z^+ > 250$ (or $\varphi_{i,i+1} < 30°$) for the three combinations of (A_o^+, f_o^+) (figure 7*a*). The result is consistent with the monotonic decline in δ_{τ_w} with growing λ_z^+, up to $\lambda_z^+ = 840$, from DNS (Du *et al.* 2002). Note that δ_{τ_w} is not necessarily the minimum at $\varphi_{i,i+1} = 0°$ (figure 7*b*).

The transverse motion speed, w_t, is a key parameter for spanwise wall oscillation and travelling wave control techniques (Karniadakis & Choi 2003). For the former,

w_t is determined from f_o and the peak-to-peak amplitude (Δz) of the oscillating wall, i.e. $w_t = (\Delta z)\pi f_o$; for the latter, w_t is given by $\lambda_z f_o$. Choi (2002) showed that all the available data of drag reduction based on spanwise wall oscillation, when plotted against w_t^+, collapsed onto one single curve; the optimum w_t^+ was 15 when skin-friction drag was reduced by 45 %. The optimum 'equivalent spanwise wall velocity', $w_{t,eq}^+$, was found to be 12 for the spanwise oscillating Lorentz force, corresponding to approximately 40 % drag reduction (Berger *et al.* 2000; Pang & Choi 2004). At $w_t^+ = 16.8$, the transverse travelling wave produced 30 % drag reduction (Du *et al.* 2002), close to that found when using spanwise oscillating Lorentz force or wall. This is reasonable because the travelling wave became an oscillatory force as its wavelength approached infinity (Karniadakis & Choi 2003). The present w_t^+ is approximately 97, approximately six times that for other techniques, at $A_o^+ = 1.94$, $f_o^+ = 0.39$ and $\lambda_z^+ = 250$, corresponding to $\delta_{\tau_w} = -35 \%$ at $x^+ = 35$. This large w_t^+ is linked to the present large f_o^+, which results from the smaller effective wavelength of the non-ideal wave than that of the ideal wave. Du *et al.* (2002) ascribed the larger f_o^+ to faster sweeping across flow required by the non-ideal wave than by the ideal wave in order to suppress the near-wall streaks and thus to achieve large drag reduction.

4.2. *Downstream recovery and spanwise variation of local wall shear stress*

The present perturbation is imposed locally. One expects that δ_{τ_w} depends on the measurement location, which is indeed confirmed in figure 8. At $x^+ = 17$ and $z^+ = 0$, δ_{τ_w} reaches more than -50% (figure 8a). The corresponding H_{12} values are 1.46 and 1.42 with and without perturbations, respectively, an indicator of no flow separation (e.g. Simpson, Strickland & Barr 1977); both occur in the unseparated region of the H_{12} versus $\delta_1/\delta_{0.995}$ plot (Sandborn & Liu 1968; Simpson, Chew & Shivaprasad 1981), where δ_1 and $\delta_{0.995}$ are boundary-layer displacement and disturbance thicknesses, respectively. As x^+ increases to 52, δ_{τ_w} climbs rapidly, but slows down for larger x^+ and approaches zero at $x^+ \approx 160$. The flow recovery to its natural state originates from a relaxation of the altered flow itself and also the entrainment of the natural flow around the control area into the perturbed region. It is worth pointing out that the present longitudinal perturbation range is very limited; only one row of actuators was deployed and the streamwise dimension of the actuators is 20 mm, only one-seventh of the longitudinal spacing (~ 140 mm) of the near-wall streaks under the present experimental condition. Further, as shown in figure 4(*a*), only the actuator tip perhaps reached the optimum amplitude of oscillation. Thus, the actuator disturbance to flow is very limited longitudinally; the controlled flow recovers rather rapidly downstream (figure 8). Park, Park & Sung (2003) achieved a maximum drag reduction up to 75 % at $x^+ = 20$ downstream of a localized periodic blowing and suction at $f_o^+ = 0.088$, though the drag recovered rapidly to the value of its natural state at about $x^+ = 130$. At $f_o^+ = 0.044$ and 0.066, their maximum drag reduction and recovery distance both retreated. Tardu & Doche (2009) obtained a maximum drag reduction of 45 % immediately downstream of a sinusoidally oscillating blowing slot. Their drag reduction diminished to less than 5 % at about $x^+ = 200$ downstream of the slot. The rapid recovery was ascribed to the advection of coherent spanwise vortices generated by the periodic blowing (Tardu 2001).

It is also of interest to examine the spanwise variation in δ_{τ_w}. In figure 8(*b*), $\delta_{\tau_w}^*$ exhibits a tooth-like variation, where the superscript '$*$' indicates normalization of δ_{τ_w} by its spanwise-average value (-23%). Here, δ_{τ_w} is in general larger between adjacent actuators than at the symmetry plane of each actuator. This observation is not unexpected in view of the deployment of discrete actuators.
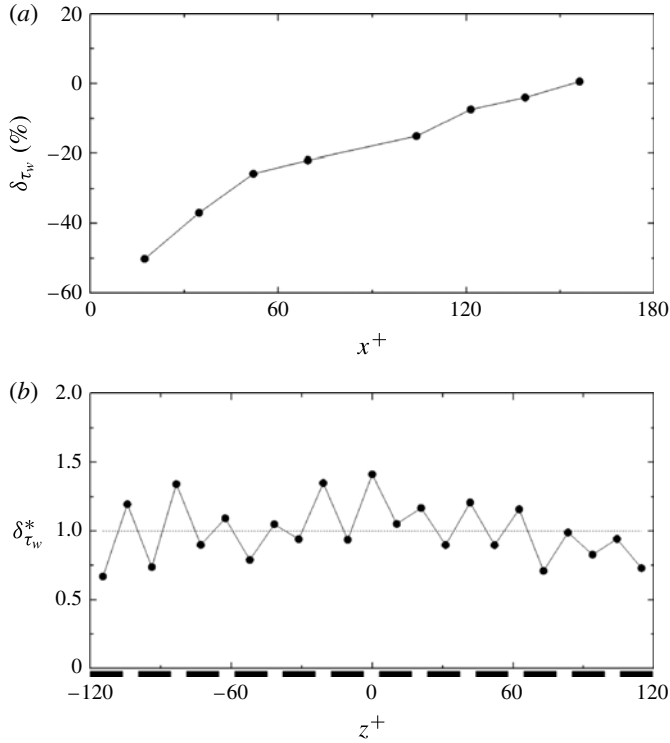
FIGURE 8. Dependence of δ_{τ_w} on (*a*) x^+ at $z^+ = 0$ and (*b*) z^+ at $x^+ = 35$ (the superscript asterisk indicates normalization of δ_{τ_w} by its spanwise-averaged value). The control parameters are $A_o^+ = 1.94$, $f_o^+ = 0.39$ and $\lambda_z^+ = 416$ (or $\varphi_{i,i+1} = 18°$). Here $U_\infty = 2.4$ m s^{-1}. The solid rectangles along the z^+ axis in panel (*b*) show the actuator locations (12 elements only).

5. Alterations to the flow structure

5.1. *Statistics of streamwise velocity*

In the absence of control, the $\overline{U}^+$ profile follows the universal law well, as indicated by the solid lines in figure 9(*a*) (Schlichting & Gersten 2000); the maximum u_{rms}^+ (figure 9*b*), around 2.6, occurs at $y^+ \approx 12$, where $S_u = 0$ (figure 9*c*) and K_u (figure 9*d*) reaches the minimum. The results suggest a fully developed TBL at the planned actuation location. Once control is introduced, the distributions of $\overline{U}^+$, u_{rms}^+, skewness S_u and kurtosis K_u of u under control, normalized by the actual wall variables, are all considerably modified. At $A_o^+ = 1.94$, $f_o^+ = 0.39$ and $\lambda_z^+ = 416$ ($\varphi_{i,i+1} = 18°$), under which δ_{τ_w} is -35% at $x^+ = 35$ and $z^+ = 0$, the linear region of $\overline{U}^+$ is extended to $y^+ \approx 14$ (figure 9*a*), in distinct contrast with $y^+ \approx 7$ without control. The observation is fully consistent with previous reports (e.g. Jung, Mangiavacchi & Akhavan 1992; Choi *et al.* 1998; Karniadakis & Choi 2003) that the drag reduction in a manipulated TBL is associated with a thickened viscous sublayer. The logarithmic region is shifted upwards, which is consistent with drag reduction. Note that the buffer region (figure 9*a*) with control becomes much thinner than the natural one, as a result of the increased viscous-sublayer thickness. Since the buffer region plays a dominant role in energy and momentum transfer between inner and outer regions as well

as in the turbulence production of the entire TBL (Kline *et al.* 1967), its reduced thickness implies that this role is impaired. The reduced buffer-layer thickness, along with a thickened viscous sublayer, was observed wherever a significant drag reduction was achieved (e.g. Choi 1989; Jung *et al.* 1992; Choi *et al.* 1998; Tardu 2001). The u_{rms}^+ was reduced at $y^+ < 8$ but increased at $8 < y^+ < 20$ (figure 9b), compared with the uncontrolled TBL. The increased u_{rms}^+ is ascribed to the actuator disturbance (figure 5c,d). This increase was also observed by Itoh *et al.* (2006). On the other hand, the reduced u_{rms}^+ in the near-wall region results from suppressed turbulence activities under manipulation, as noted when a significant drag reduction was achieved with a riblet wall (Choi 1989; Choi, Moin & Kim 1993), spanwise wall oscillation (Jung *et al.* 1992; Laadhari, Skandaji & Morel 1994; Choi *et al.* 1998), a transverse travelling wave (Du & Karniadakis 2000; Du *et al.* 2002), and local oscillating blowing (Tardu 2001). Correspondingly, S_u (figure 9c) below the zero-crossing point, i.e. $y^+ = 12$, is larger than its uncontrolled counterpart, that is, U in the viscous region is more positively skewed. This may imply a drop in the events of large positive U and hence in $\overline{U}$, thus suggesting weakened high-speed streaks. This interpretation is supported by the reduced u_{rms}^+ at $y^+ < 8$ (figure 9b) and also conforms to the measured drag reduction. In the buffer region, S_u is slightly lower with control than that without, which echoes an increased u_{rms}^+ in this region (figure 9b). However, S_u remains almost unchanged in the log-law region. Under spanwise wall oscillation (e.g. Choi *et al.* 1998) and local oscillating blowing (Tardu 2001), S_u displayed a considerable departure from that uncontrolled in both the linear and buffer regions but not in the log-law region. At $y^+ < 10$, K_u increases as a result of control (figure 9d). This is expected since the wall-based oscillation acts to enhance exchange activities between low- and high-speed fluid regions. The minimum K_u occurs at $y^+ \approx 12$, corresponding to the zero-crossing point of S_u (figure 9c). Similarly to S_u, the change in K_u is barely noticeable in the log-law region. In the outer-layer region, i.e. $y^+ > 200$, u_{rms}^+, S_u and K_u (figure 9b–d) differ appreciably with control from their counterparts without; their profiles appear shifted towards the wall. This is due to the normalization in figure 9 by the actual wall variables.

5.2. *Streaky structures*

The flow structure was examined both qualitatively and quantitatively, with emphasis on low-speed streaks and streamwise vortices near the wall, in order to gain some insight into the mechanism behind the observed drag reduction. In this section, unless otherwise stated, the perturbation was produced with $A_o^+ = 2.22$, $f_o^+ = 0.65$ and $\lambda_z^+ = 416$ ($\varphi_{i,i+1} = 18°$). Figure 10 presents typical photographs of instantaneous near-wall flow structures from the smoke–wire flow visualization in the *xz* plane at $y^+ = 10$. In the absence of control, high- and low-speed streaks lying side by side are evident (figure 10a). The average spanwise spacing between low-speed streaks is approximately 100 wall units, in agreement with Kline *et al.*'s (1967) hydrogen bubble visualization. Movie clips (not shown) indicate that smoke filaments from the smoke–wire placed at $y^+ = 8$ become entangled and are raised to form thick longitudinal smoke tubes. These tubes, which tend to slow down and form low-speed streaks, are illuminated by the laser sheet when rising from the wall. On both sides of the low-speed streak, a pair of counter-rotating streamwise vortices, denoted by the curled arrows in figure 10(a), pump low-momentum fluid away from the wall. Meanwhile, on the downdraught side of the streamwise vortices, high-momentum
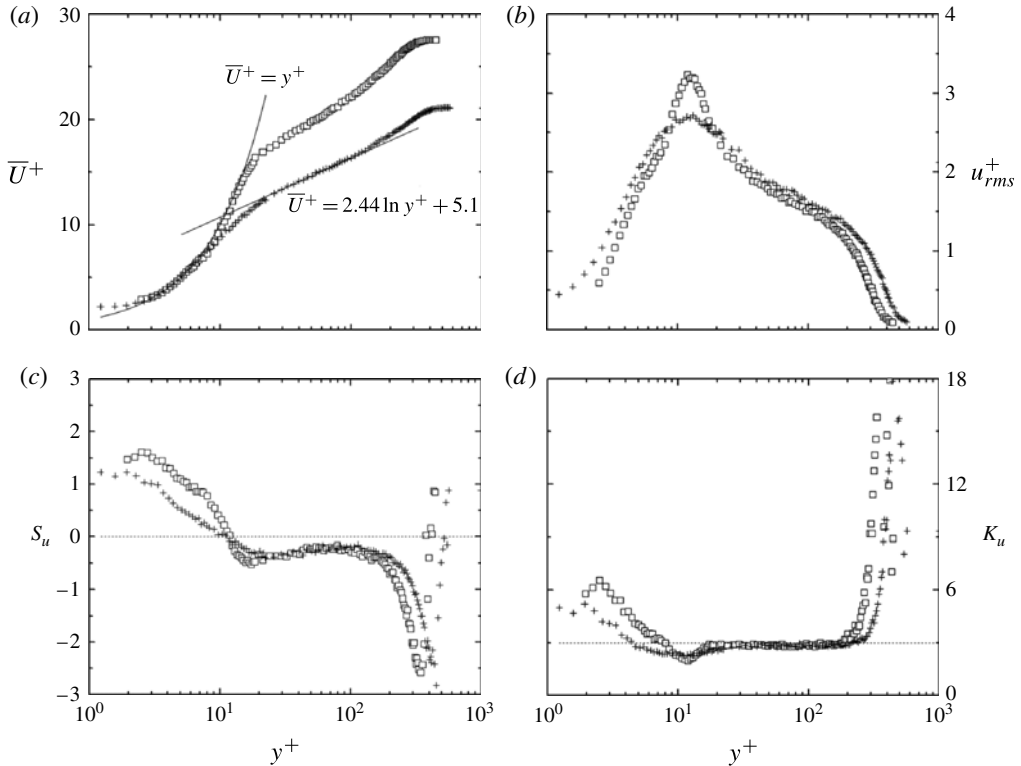
FIGURE 9. Distributions of (*a*) mean streamwise velocity $\overline{U}^+$ of U; (*b*) r.m.s. value u^+_{rms}; (*c*) skewness S_u; and (*d*) kurtosis K_u: +, without control; $\square$, with control. The control parameters are as in figure 8. Here $U_\infty = 2.4$ m s^{-1}.

fluid is induced towards the wall, forming high-speed streaks, which are missed by the laser sheet, thus appearing as dark areas in the photograph. However, with control, the large-scale streaky structures are no longer observable; instead, more stable and smaller-scale longitudinal structures appear, which are more coherent and elongated in the streamwise direction (figure 10*b*). The PIV-measured instantaneous u^+ distributions in the xz plane at $y^+ = 5.5$ (not shown here) have also confirmed that, when control is applied, the spacing between low-speed streaks becomes smaller and the length of these streaks becomes larger than of the high-speed streaks.

The streaks in figure 10(*b*) differ in appearance from those observed in the DNS data for either the transverse travelling wave (Du & Karniadakis 2000; Du *et al.* 2002) or the spanwise oscillatory Lorentz force (e.g. Berger *et al.* 2000). There are also differences in detail from what has been observed over riblets (e.g. Choi 1989) or a spanwise oscillating wall (e.g. Choi *et al.* 1998), where drag reduction was achieved. There is however an unmistakable feature common to all the visualizations associated with significant drag reduction, *viz.* the streaky structure is more ordered than in the natural case. It would appear that this increased organization is a generic feature of the near-wall flow produced by a variety of drag reduction strategies, although in each case the mechanisms underpinning the drag reduction may differ. For example, we note that the streaks in figure 10(*b*) are quite similar in appearance to those observed on a smooth wall immediately downstream of a suction strip (see e.g. figure 10(*b*) in
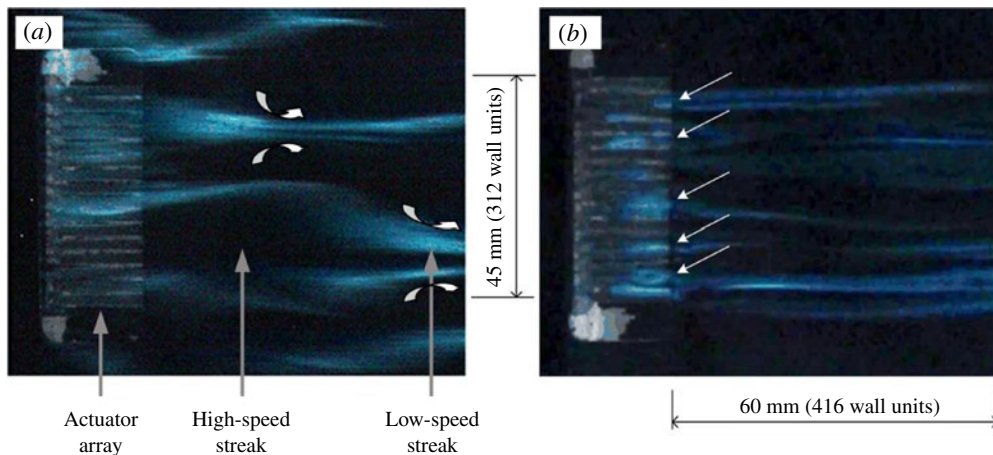
FIGURE 10. (Colour online) Typical photographs of instantaneous flow structure in the xz plane at $y^+ = 10$ from smoke–wire flow visualization: (*a*) uncontrolled, (*b*) controlled. Control parameters: $A_o^+ = 2.22$, $f_o^+ = 0.65$ and $\lambda_z^+ = 416$ (or $\varphi_{i,i+1} = 18°$). Flow at $U_\infty = 1.5$ m s^{-1} is left to right. Curled arrows in panel (*a*) indicate streamwise vortices. Normal arrows in panel (*b*) point to twisted smoke filaments at the actuator tips.

Antonia *et al.* (1988)). When the suction is sufficiently strong, relaminarization occurs (Antonia, Zhu & Sokolov 1995), the orderly/stabilized streaks being observable almost until their final disappearance, i.e. when the flow returns to a laminar state.

The near-wall streaky structures are statistically studied based on the PIV-measured u^+ in the xz plane at $y^+ = 5.5$. Following Schoppa & Hussain (2002) and Iuso *et al.* (2003), the low-speed streaks in the near-wall region were identified with their centres, width, spacing and strength. The length of the streaks, however, cannot be determined due to the limited PIV measurement area (306 wall units $\times$ 306 wall units). Briefly, (i) detect the low-speed streaks characterized by $u^+ < 0$, (ii) determine the streak centre by the location of the local minimum u^+ along every z cut through the plane, (iii) make the zero-crossing point in z of u^+ as the streak edge, and (iv) calculate the local maximum of $|\partial u^+/\partial z^+|$ in z on either side of the streak centre and take the larger value as the streak strength. Table 2 compares the streaky structures with and without control. The control increases the centre number of low-speed streaks by approximately 15 %, but reduced both the averaged width and spacing by approximately 12 %. Figure 11 presents the histograms of the spacing and width of low-speed streaks. Evidently, both the spacing and width distributions with control are shifted towards lower values, internally consistent with the observation from flow visualization, where longitudinal structures with control are overwhelmingly reduced in size but increased in number.

There is a difference between our data and those of Iuso *et al.* (2003), which is linked to the difference between the two approaches used. The present discrete actuators generate more organized smaller-scale longitudinal structures in the near-wall region, along with a greater number of narrower regions of negative u^+ or low-speed streaks. Naturally, the number of identified low-speed streaks increases in the controlled flow, associated with the diminished streak width and spacing (table 2, figure 11) but the larger spanwise gradient of velocities, which accounts for a growth in the streak strength (table 2). On the other hand, the low-speed streaks coalesce

	Natural TBL	Disturbed TBL
No. of identified centres	294 653	337 704
Averaged streak width (wall units)	49.2	43.2
Averaged streak spacing (wall units)	83.8	72.5
Averaged streak strength (wall units)	0.278	0.314

TABLE 2. Statistical results of low-speed streaks at $y^+ = 5.5$.
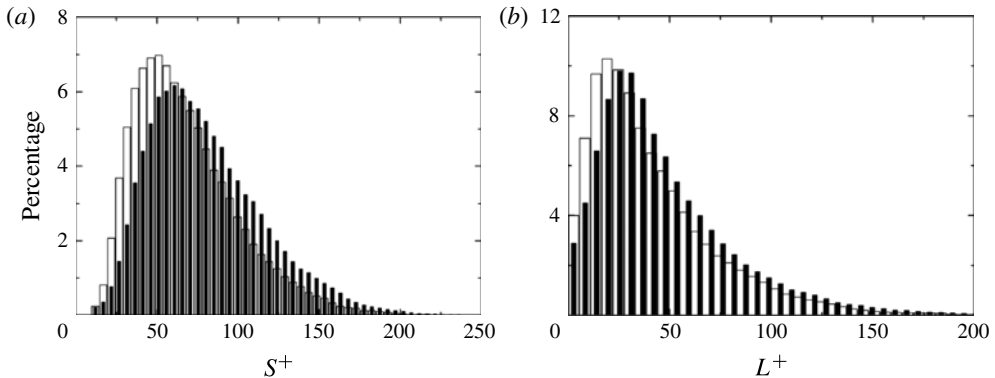
FIGURE 11. Histograms of (*a*) spacing S^+ and (*b*) width L^+ of low-speed streaks: ■, uncontrolled; □, controlled. Analysis is based on the PIV data in the xz plane of $y^+ = 5.5$. Control parameters are as in figure 10. Here $U_\infty = 2.4$ m s^{-1}.

under the spanwise oscillation of the entire wall, forming fewer and wider low-speed streaks with increased spacing (Choi *et al.* 1998; Iuso *et al.* 2003). Iuso *et al.* (2003) observed a drop by 20 % in the number of low-speed streaks, increases by 37 % in the streak width and by 17 % in the streak spacing, but a decrease by 15 % in the streak strength.

At the edges of the streak, $\partial u/\partial x$ is associated with the so-called internal shear layer (Blackwelder & Haritonidis 1983; Johansson *et al.* 1991) as well as with the generation of streamwise vortices due to the streak instability (Schoppa & Hussain 2002). The histogram of $\partial u^+/\partial x^+$ (figure 12) at the edge of the streak appears positively skewed without control since positive $\partial u^+/\partial x^+$ is weakened when fluid particles cross the edge of the streak (Iuso *et al.* 2003). With control, the histogram appears more symmetrical about $\partial u^+/\partial x^+ = 0$ owing to fewer coherent structures (Iuso *et al.* 2003), which is consistent with figure 10. The higher occurrence of large $|\partial u^+/\partial x^+|$ under control may suggest that the low-speed streaks become more misaligned with the streamwise direction and probably more wavy, as observed under spanwise wall oscillation by Iuso *et al.* (2003).

The near-wall fluctuating streamwise vorticity, $\omega_x = \partial w/\partial y - \partial v/\partial z$, estimated from PIV measurements in the yz plane at $x^+ = 35$, is shown in figure 13. In the absence of control, streamwise vortex pairs, i.e. A_1–A_2, B_1–B_2 and C_1–C_2 in figure 13(*a*), may be easily identified from the streamwise vorticity and velocity vectors. Once control is introduced, there is a discernible change (figure 13*b*). Firstly, smaller-scale vortices appear in the region $y^+ \approx 0$ to $y^+ \sim 30$. Secondly, the centroids of these vortices tend to lie along a wavy (along z) trajectory whose wavelength is approximately equal to the span of the array of actuators. Thirdly, the small-scale vortices appear to rotate
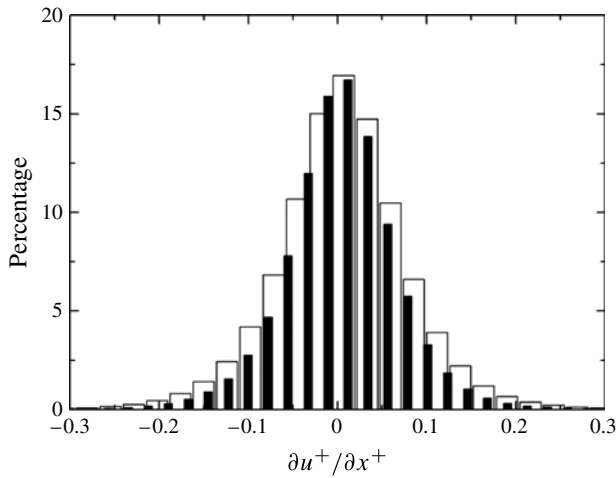
FIGURE 12. Histograms of $\partial u^+/\partial x^+$ at the borders of low-speed streaks: ■, uncontrolled; □, controlled. Analysis is based on the PIV data in the xz plane of $y^+ = 5.5$. Control parameters are as in figure 10. Here $U_\infty = 2.4$ m s^{-1}.
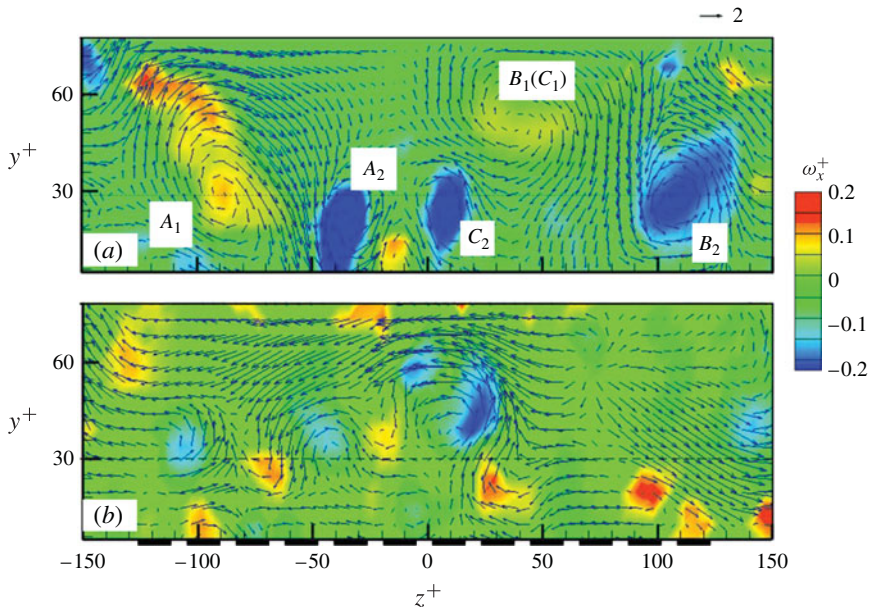

FIGURE 13. Instantaneous fluctuating streamwise vorticity ω_x^+ and velocity vectors (v^+, w^+) in the yz plane at $x^+ = 35$ in (a) the absence and (b) the presence of control. Control parameters are as in figure 10. The reference vector length equals 2 wall units. Here $U_\infty = 2.4$ m s^{-1}. The solid rectangles along the z^+ axis indicate the locations of the actuators.
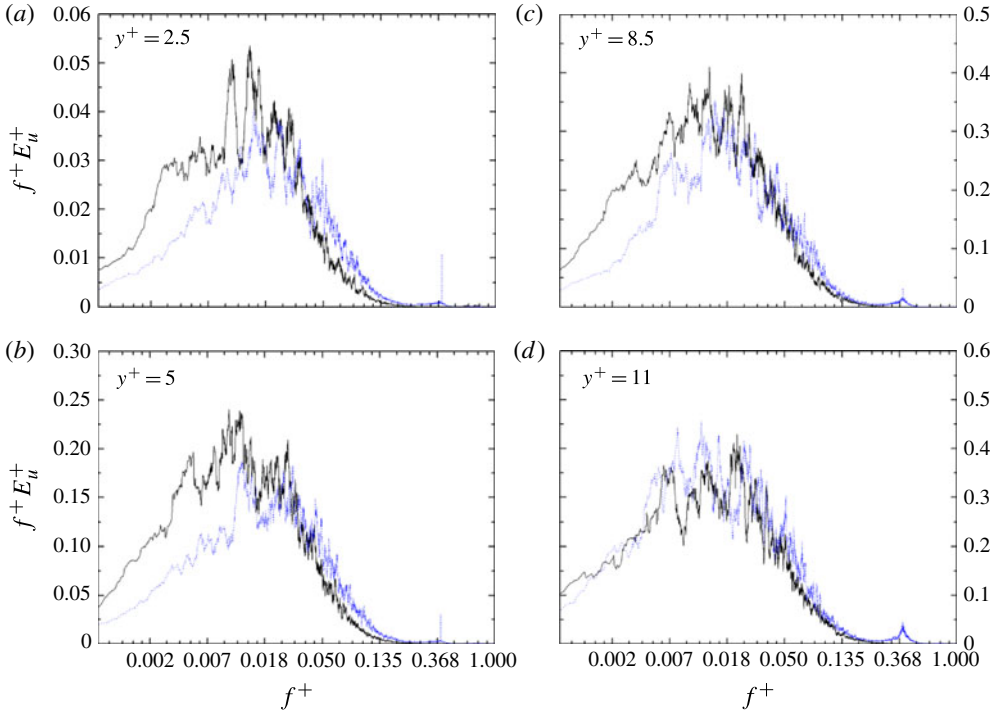
FIGURE 14. (Colour online) Power spectra of the hot-wire-measured fluctuating velocity u at (a) $(x^+, y^+, z^+) = (35, 2.5, 0)$, (b) $(35, 5, 0)$, (c) $(35, 8.5, 0)$ and (d) $(35, 11, 0)$: solid line, uncontrolled; dotted line, controlled. A natural log scale is used for the abscissa. Control parameters are as in figure 8. Here $U_\infty = 2.4$.

in the same direction, as indicated by the positive-ω_x^+ distributions that are seen in the wall region. Fourthly, the larger-scale vortices occur mostly away from the wall. The observations are internally consistent with the smoke–wire flow visualization (figure 10); on the basis of viewing movie clips, the smoke filaments are twisted immediately at the actuator tips, as indicated by the arrows in figure 10(b), to form a layer of highly regularized streamwise vortices. It appears that the streamwise vortices generated by the actuators act as a barrier between the large-scale streamwise vortices and the wall, thus making it more difficult for the sweep motions to reach the wall.

6. Discussion

6.1. *Redistributed energies of turbulent structures*

The power spectral density function, E_u, of u measured in the viscous sublayer and buffer layer ($x^+ = 35$, $z^+ = 0$) is examined. The function E_u was calculated in such a way that its integration over the entire frequency range yields the variance of u, i.e. $\int_{-\infty}^{\infty} E_u \, df = \lim_{T\to\infty} (1/T) \int_{-\infty}^{\infty} u^2 \, dt$. In figure 14, E_u^+ is multiplied by f^+ so that the distribution of $f^+ E_u^+$ is centred about the most energetic frequencies. Further, in order to infer how much energy each frequency contributes to $\overline{u^2}$, the product $f^+ E_u^+$ is plotted against f^+ in figure 14 (a natural log scale is used for the abscissa). In the absence of control, the distribution of $f^+ E_u^+$ is mainly concentrated in the range of $f^+ \approx 0.002$–0.03. The imposed value of f_o^+ is in the dissipative range of the u

spectra. There is a discernible peak at $f^+ = f_o^+ = 0.39$ with control; this peak broadens with increasing y^+. It is evident that the actuator affects the low-frequency end of the spectra very near the wall (figure 14a–c); at $y^+ = 11$ (figure 14d), the effect has virtually disappeared. With control, when $y^+ < 11$ (figure 14a–c), $f^+ E_u^+$ decreases considerably for $f^+ < 0.04$ and increases for $f^+ > 0.04$, indicating an energy transfer from large- to small-scale turbulent structures. Similar observations about the energy transfer were also made in other control techniques. For example, Choi (2002) found, based on a spanwise wall oscillation, that the power spectra decreased and increased for f^+ smaller and larger than the wall-oscillation frequency, 0.0125, respectively, which was lower by far than the present one. Interestingly, the energy spectra of wall skin-friction and wall pressure fluctuations over a riblet wall also showed similar changes under control (Choi 1989). The increased energy in higher frequencies was ascribed to an increase in the bursting frequency over the riblet surface. The riblets restricted the lateral movement of longitudinal vortices, thus resulting in a decrease in the energy of lower frequencies. Iuso *et al.* (2002) manipulated a turbulent channel flow using spanwise-arrayed inclined wall jets, which generated streamwise vortices, and observed that the spectra of both wall skin-friction fluctuation and u shifted towards the lower frequency range. They interpreted this result as a manifestation of an increase in the length of velocity streaks, which might result from the increased stability of the controlled flow.

6.2. *Weakened bursting events*

The bursting frequency f_b^+ may be detected from the u signal with the variable-interval time-average (VITA) technique (Blackwelder & Kaplan 1976). The acceleration process, which reflects better the bursting phenomenon than the deceleration, is examined by setting $\mathrm{d}u(t)/\mathrm{d}t > 0$ for the VITA criterion (Chen & Blackwelder 1978; Antonia & Bisset 1990). The bursts detected using VITA depend on the threshold k and the averaging duration T^+ (Blackwelder & Kaplan 1976). As illustrated in figure 15(a), with u measured at $x^+ = 35$, $y^+ = 5$ and $z^+ = 0$, f_b^+ decreases gradually with increasing k, as observed by Blackwelder & Kaplan (1976) and Alfredsson & Johansson (1984). The magnitude of f_b^+ is reduced under control, irrespective of the choice of k. The effect of T^+ on f_b^+ (figure 15b) is rather different. With increasing T^+, f_b^+ increases rapidly at first but decreases slowly after reaching its maximum at $T^+ = 15$ and 23 for cases with and without control, respectively. Beyond $T^+ = 23$, f_b^+ drops significantly with control. Note that f_b^+ is larger at $T^+ < 23$ with than without control, which is ascribed mainly to perturbation-generated relatively small-scale structures, i.e. the streamwise vortices introduced by the actuators. As shown in the spectral analyses, small-scale structures are excited with control so that the local variance of u over a small T^+ (corresponding to the small-scale structures of high frequency) becomes larger. Choi (1989) noted an increase in f_b^+ over a riblet wall as well as an increase in high-frequency energy of the skin-friction spectrum. Iuso *et al.* (2002) investigated the effect of T^+ on f_b^+ and observed, when T^+ was significantly small, a rapid decline in the difference between the controlled and uncontrolled values of f_b^+. A similar observation was also made by Di Cicca *et al.* (2002).

The present values of k and T^+ are set at 0.8 and 38, respectively, for which the identification of the bursts seemed reasonable by comparison with the visual detections from the u signal. Figure 16 presents the variation in f_b^+ with y^+ ($\leqslant 10$). In the natural TBL, at $y^+ < 8$, the detected f_b^+ rises slowly with y^+, as previously observed by Blackwelder & Haritonidis (1983). However, when the control is applied,
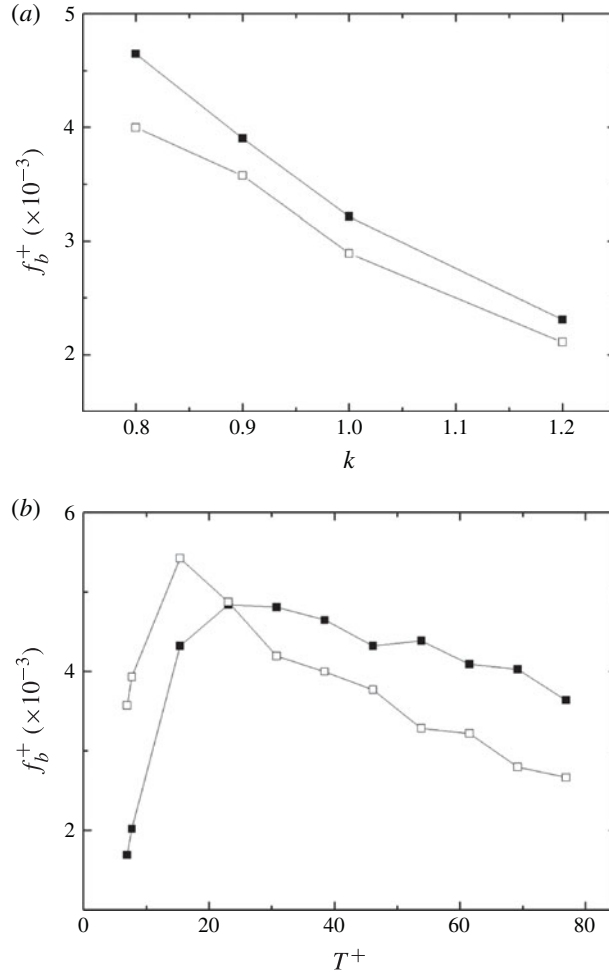
FIGURE 15. Dependence of the bursting frequency f_b^+, detected from the hot-wire signal measured at $(x^+, y^+, z^+) = (35, 5, 0)$, on the VITA parameters, for (*a*) $T^+ = 38$ and (*b*) $k = 0.8$: ■, uncontrolled; □, controlled. Control parameters are as in figure 8. Here $U_\infty = 2.4$ m s^{-1}.

f_b^+ becomes considerably smaller throughout the y^+ range. For instance, at $y^+ = 3.6$ and 6.5, f_b^+ is reduced by 18 % and 21 %, respectively, relative to the uncontrolled case. This reduction indicates a suppression of turbulence activity in the near-wall region, contributing to drag reduction (e.g. Karniadakis & Choi 2003).

Distributions of $\langle u^+ \rangle$, where the angular brackets denote ensemble averaging based on VITA detections, are presented in figure 17. The magnitude and duration of the burst diminish by approximately 13 % and 23 %, respectively, with control, independently of y^+. The result implies a stabilization of the low-speed streaks and a weakened stretching of the vortices if we accept the relationship that exists between velocity streaks and streamwise vortices (e.g. Karniadakis & Choi 2003). It also implies a suppression of turbulence activity. Using periodic spanwise wall oscillation, Choi & Clayton (2001) achieved a drag reduction of 45 %. This was accompanied by
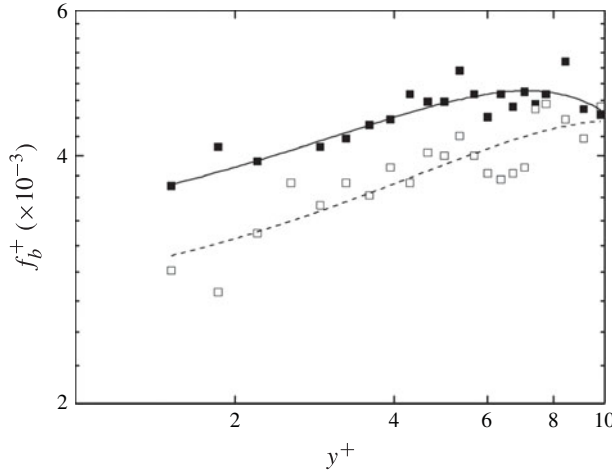
FIGURE 16. Variation with y^+ of the bursting frequency f_b^+ detected using VITA from the hot-wire signal placed at $(x^+, y^+, z^+) = (35, y^+, 0)$: ■, uncontrolled; □, controlled. Control parameters are as in figure 8. The solid and dashed lines are parabolic fits to estimated f_b^+ with and without control, respectively. VITA parameters: threshold $k = 0.8$ and averaging time $T^+ = 38$. Here $U_\infty = 2.4$ m s^{-1}.

a reduction of nearly 33 % in the duration and approximately 20 % in the intensity of the burst.

6.3. *Increased energy dissipation and Taylor microscale*

Figure 18 presents the variation with y^+ of $\overline{(\partial u^+/\partial x^+)^2}$, one component of the mean energy dissipation rate, with and without control. The variance of $\overline{(u^+)^2}$ is also included in figure 18 to facilitate the interpretation of the data. The spatial derivative $\partial u/\partial x$ was estimated via Taylor's hypothesis using a measured constant convective velocity (12 wall units) in the near-wall region. In the absence of control, $\overline{(\partial u^+/\partial x^+)^2}$ grows progressively with increasing y^+ until $y^+ = 30$, while $\overline{(u^+)^2}$ reaches its maximum at $y^+ \approx 12$. Once the control is applied, $\overline{(\partial u^+/\partial x^+)^2}$ climbs more rapidly than without control with increasing y^+, resulting in an increase in $\overline{(\partial u^+/\partial x^+)^2}$ with control. After reaching the maximum at $y^+ \approx 12$, however, the controlled $\overline{(\partial u^+/\partial x^+)^2}$ declines with a further increase in y^+ ($\leqslant 20$). Perhaps not surprisingly, both the controlled $\overline{(\partial u^+/\partial x^+)^2}$ and $\overline{(u^+)^2}$ return to their uncontrolled values at $y^+ > 20$, implying that an internal layer, consisting of the introduced streamwise vortices, has been generated by the present wall-based perturbation. Further, this may suggest that the introduced layer of streamwise vortices is highly dissipative. In fact, the increased energy dissipation rate in the near-wall region can be easily seen in figure 19, where the variation of $f^{+2}E_u^+$ with f^+ is shown at different y^+ locations in the near-wall region. With control, the distribution of $f^{+2}E_u^+$ shows a pronounced peak at $f^+ = 0.39$. This peak becomes broader with increasing y^+. Obviously, this peak is due to the imposed oscillation of the actuators and reflects the increased mean energy dissipation rate in the near-wall region when the control is applied. This is consistent with figure 18. Clearly, the increased energy dissipation rate in the near-wall region also contributes to the significant drag reduction.
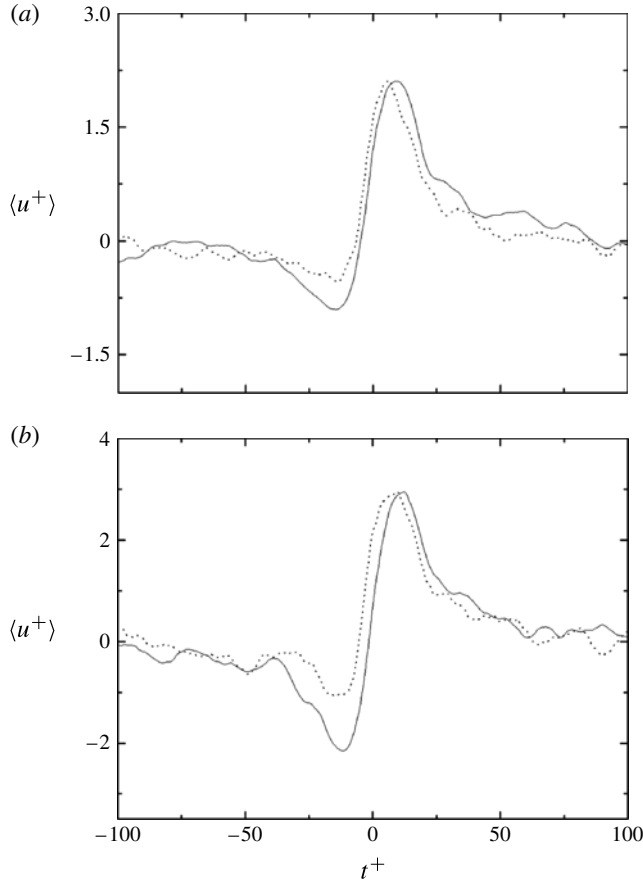
FIGURE 17. Ensemble-averaged streamwise fluctuating velocity, $\langle u^+ \rangle$, based on VITA detections from the hot-wire signal measured at (*a*) $(x^+, y^+, z^+) = (35, 3.5, 0)$ and (*b*) $(35, 6.5, 0)$: solid line, uncontrolled; dotted line, controlled. Control parameters are as in figure 8. VITA parameters: $k = 0.8$ and $T^+ = 38$. Here $U_\infty = 2.4$ m s^{-1}.

The Taylor microscale has been estimated with and without control in order to examine the effect of control on the fine turbulent structures. The Taylor microscale is defined as $\lambda_T = \sqrt{2\overline{u^2}/\overline{(\partial u/\partial t)^2}}$ and is a hybrid scale since it contains information on both large scales via $\overline{u^2}$ and small scales via $\overline{(\partial u/\partial t)^2}$. Without control, λ_T^+ (figure 20) increases away from the wall to a maximum at $y^+ \approx 5$ and then declines gradually with increasing y^+, in conformity with the result of Nagano, Tsuji & Houra (1998) and Metzger (2006). At $y^+ = 8$, λ_T^+ is approximately 8.3, in good agreement with Tardu's (2001) measurement in a natural boundary layer. With control, λ_T^+ is markedly reduced in the sublayer and part of the buffer region. It has a peak at $y^+ = 5$, which is nearly a factor of 2 smaller than in the natural TBL. For $y^+ \geqslant 15$, λ_T^+ is almost indistinguishable from that in the natural TBL. The significant reduction in λ_T^+ in the near-wall region (i.e. $y^+ \leqslant 15$) is due to the increase in $\overline{(\partial u/\partial t)^2}$, with a smaller contribution from the reduced $\overline{u^2}$, which is consistent with the reduction in f_b^+ (figure 16). The latter represents an increase in one (the isotropic) component of the dissipation rate, which is indeed confirmed in figures 18 and 19. Tardu (2001) found
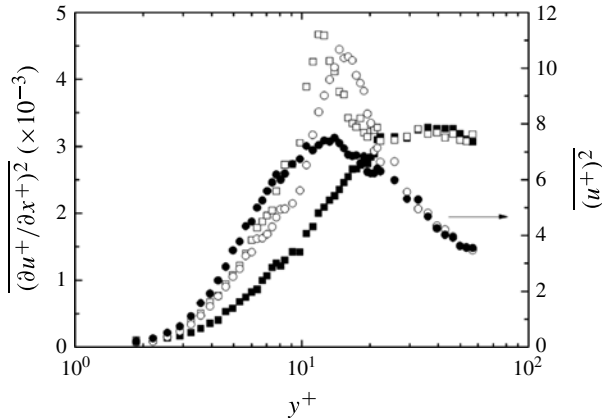
FIGURE 18. Variations with y^+ of energy dissipation rate $\overline{(\partial u^+/\partial x^+)^2}$ and u variance $\overline{(u^+)^2}$: ■ and ●, uncontrolled; □ and ○, controlled. Control parameters are as in figure 8. The hot-wire signal was measured at $(x^+, y^+, z^+) = (35, y^+, 0)$. Here $U_\infty = 2.4$ m s^{-1}.
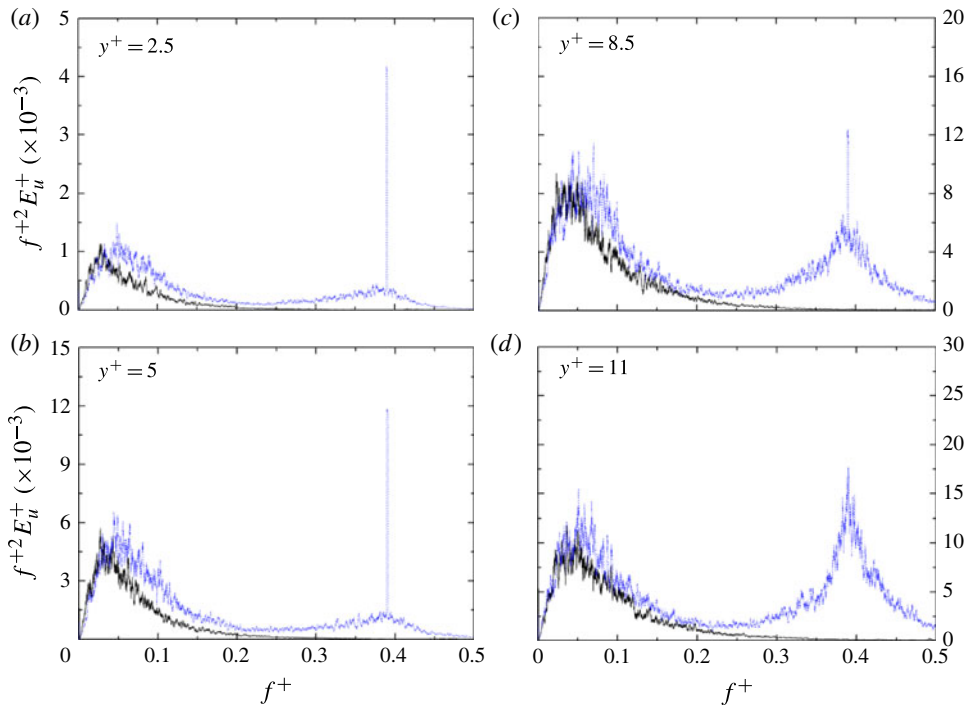

FIGURE 19. (Colour online) Variation of $f^{+2}E_u^+$ with f^+: (*a*) $(x^+, y^+, z^+) = (35, 2.5, 0)$, (*b*) $(35, 5, 0)$, (*c*) $(35, 8.5, 0)$ and (*d*) $(35, 11, 0)$: solid line, uncontrolled; dotted line, controlled. Control parameters are as in figure 8. Here $U_\infty = 2.4$ m s^{-1}.

at the end of the acceleration phase associated with a periodic blowing on the wall that the Taylor microscale was reduced by a factor of 2, while the isotropic dissipation rate was increased by a factor of 12, resulting in partial relaminarization downstream.
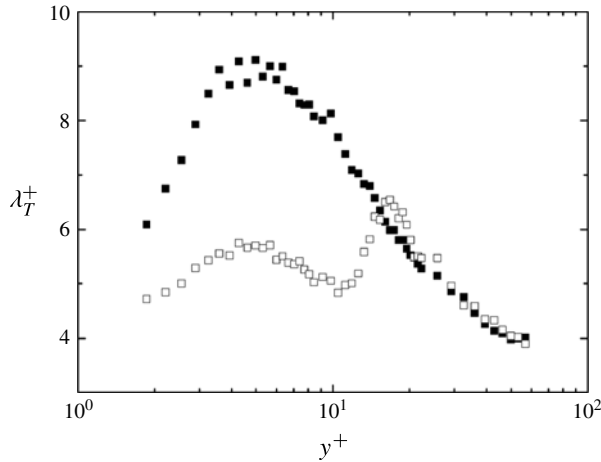
FIGURE 20. Variation with y^+ in Taylor microscale λ_T^+: ■, uncontrolled; □, controlled. Control parameters are as in figure 8. The hot-wire signal was measured at $(x^+, y^+, z^+) = (35, y^+, 0)$. Here $U_\infty = 2.4$ m s^{-1}.

Using a spanwise oscillating wall, Laadhari *et al.* (1994) achieved a skin-friction drag reduction by 40 % and observed a decrease in the Taylor microscale for $y^+ < 40$.

6.4. *Other aspects of turbulent structures*

Johansson *et al.* (1991) performed conditional averaging of shear-layer structures, inclined to the flow, in the near-wall region of a turbulent channel flow, and found that a much larger $\partial u/\partial t$ occurred when low-speed streaks were followed by high-speed ones than in the inverse situation. The characteristics of $\partial u/\partial t$ may be quantified by the skewness $(S_{\partial u/\partial t})$ and kurtosis $(K_{\partial u/\partial t})$, as shown in figure 21. In general, $S_{\partial u/\partial t}$ is greater than zero, implying a positively skewed distribution of $\partial u/\partial t$, which is attributed to the wavy nature of low-speed streaks close to the wall (Onorato & Iuso 2001). In the natural TBL, $K_{\partial u/\partial t}$ varies little with increasing y^+ (figure 21*b*). With control, the distribution of $\partial u/\partial t$ alters significantly, as reflected in $S_{\partial u/\partial t}$ and $K_{\partial u/\partial t}$. Both $S_{\partial u/\partial t}$ and $K_{\partial u/\partial t}$ increase at $y^+ < 8$ with control, though the departure from the natural case diminishes gradually with increasing y^+. This increase in $S_{\partial u/\partial t}$ and $K_{\partial u/\partial t}$ indicates that the near-wall flow structure becomes more intermittent with than without control (Iuso *et al.* 2002). In view of the weakened large-scale structures and the lower bursting frequency with control, it may be inferred that large $\partial u/\partial t$ occurs more sparsely in the near-wall region (Iuso *et al.* 2002). At $y^+ > 8$, $S_{\partial u/\partial t}$ with control falls below the natural one, reaching the minimum at $y^+ = 11$, implying less intermittency. This is reasonable because u_{rms} increases in the buffer region with control (figure 6*b*).

6.5. *Drag reduction mechanism*

In this section, we enquire into the mechanism responsible for the drag reduction (figures 6–8). As discussed in the Introduction, one expects a large wall shear stress to be closely associated with the presence of streamwise vortices. The latter, which are generally located immediately above and displaced laterally from the regions of
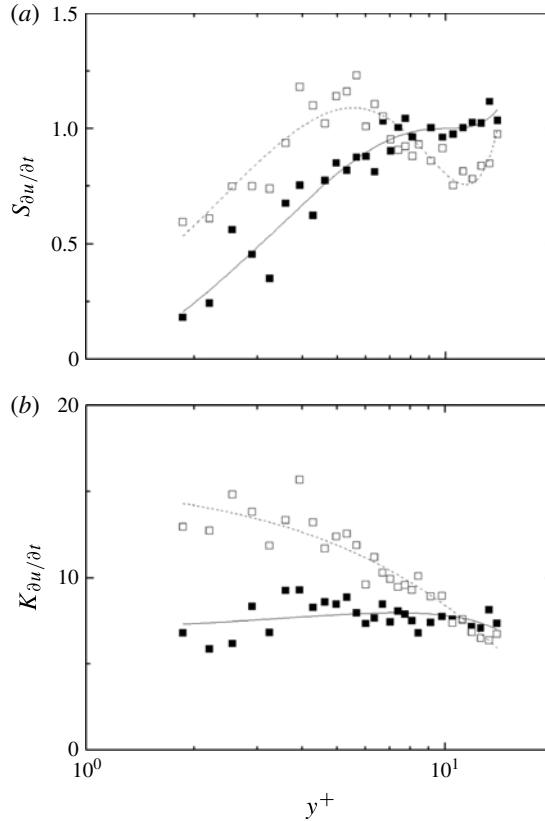
FIGURE 21. Dependence on y^+ of (*a*) the skewness and (*b*) the kurtosis of $\partial u/\partial t$:
■, uncontrolled; □, controlled. The hot-wire signal was measured at $(x^+, y^+, z^+) = (35, y^+, 0)$. Control parameters are as in figure 8. Solid and broken lines are (*a*) cubic or (*b*) parabolic fits to estimated data. Here $U_\infty = 2.4$ m s^{-1}.

high skin-friction drag, account for sweeps and ejections, bursts and streaky structures (e.g. Kim 1983). Among the events, the sweep is directly responsible for the large wall skin friction on the basis of observation. It would seem that the connection between the wall and streamwise vortices has been weakened by the present control. Following our observations in §5.2, we formally surmise here that the transverse travelling wave created by the oscillating actuators produces a wavy layer of highly regularized streamwise vortices (figure 22). This layer plays two distinct roles in the context of drag reduction. Firstly, it acts as a barrier that prevents the large-scale coherent structures from reaching the wall. It thus interferes with the turbulence production cycle, which consists largely of vortex formation, streak formation and breakdown (Kim 2011). The streak instabilities, i.e. the sinuous or outer instability and the varicose or inner instability (Marquillie, Ehrenstein & Laval 2011; Vaughan & Zaki 2011), may also be affected. The effectiveness of the barrier depends to a large extent on the strength of the streamwise vortices that the actuators introduce and on how well they are regularized. The higher the wave speed w_t^+ $(= \lambda_z^+ f_o^+)$, the more regularized should the vortices become. At the shortest wavelength $(\lambda_z^+ = 42$ or $\varphi_{i,i+1} = 180°)$, the travelling wave produces streamwise vortices and regularizes them, thus impairing the connection between the existing coherent structures and the wall
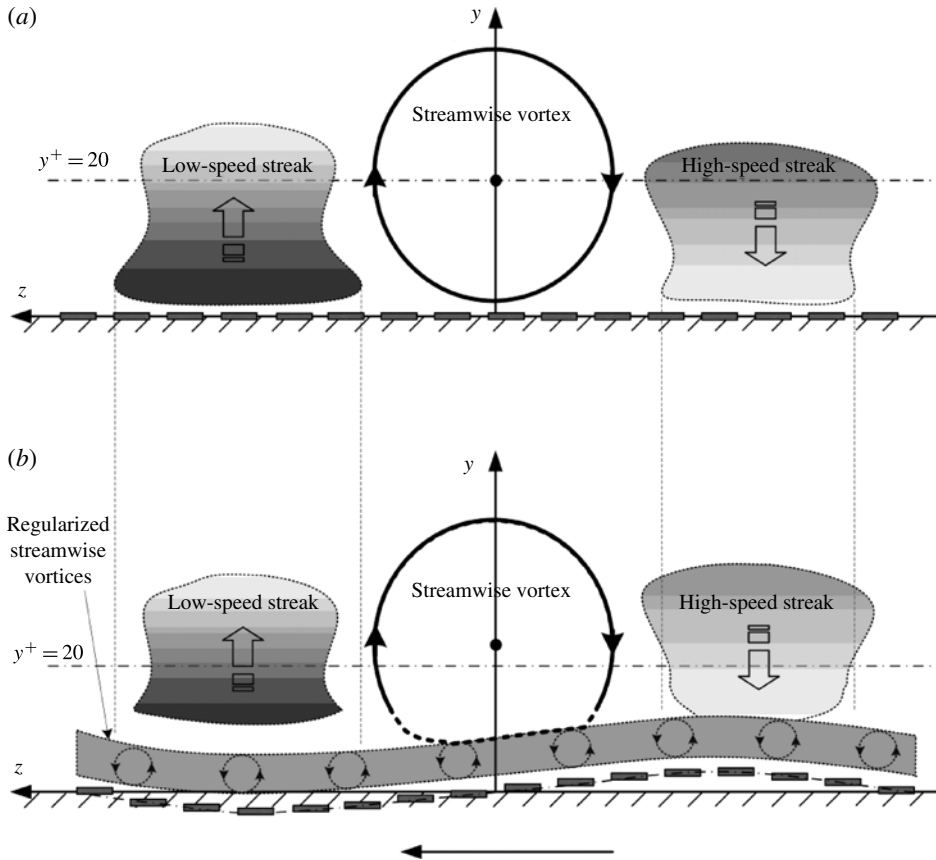
(*a*)

(*b*)

FIGURE 22. A schematic of the drag reduction mechanism: (*a*) control off; (*b*) control on. The transverse travelling wave formed by the wall-based discrete actuators generates a layer of highly regularized streamwise vortices, which acts to weaken or even break the connection between the large-scale coherent structures and the wall.

and hence reducing the drag. With increasing λ_z^+ or reducing $\varphi_{i,i+1}$, w_t^+ increases, further improving the regularization of the streamwise vortices along the spanwise direction. Therefore, this layer of streamwise vortices may act more effectively, resulting in the monotonic decline in δ_{τ_w} with increasing λ_z^+ (figure 7). The second role played by the introduced vortex layer was described in § 6.3, *viz.* the wavy layer of streamwise vortices is highly dissipative since it is associated with an increase in $\overline{(\partial u^+/\partial x^+)^2}$ and hence in the dissipation rate.

The mechanism proposed above is supported by the experimental data. Firstly, figure 10(*b*) shows a significant increase in smaller-scale but more coherent streaks in the streamwise direction and a relatively well-defined spanwise spacing. This is consistent with the production of streamwise vortices. This change is also evident in figures 11–13. Secondly, the viscous sublayer is greatly thickened with actuation (figure 9*a*), by nearly a factor of 2. Thirdly, the spectral analysis (figure 14) indicates that the relatively large-scale structures are associated with a reduced energy, as a result of control. Fourthly, the active turbulence activity, i.e. the bursting events connected to ejection and sweep motions, is considerably weakened (figures 15–17).

Fifthly, the energy dissipation rate in the near-wall region is increased with control (figures 18 and 19), which also contributes to the significant drag reduction. Finally, the Taylor microscale is reduced by more than 30 % in the near-wall region (figure 20); this is consistent with the increased energy dissipation rate in this region and the decreased frequency of ejections.

It is worth commenting on the observation that the change in δ_{τ_w} is very small beyond $\lambda_z^+ = 250$ (figure 7), irrespectively of the combination of (A_o^+, f_o^+). Realistically, even at $\varphi_{i,i+1} = 0°$ (or $\lambda_z^+ \to \infty$), the fluid motion induced by discrete actuators cannot be entirely in phase due to the finite gap between adjacent actuators, implying that the corresponding effective λ_z^+ cannot be infinite. The maximum effective wavelength is presently estimated to be only approximately 250 based on figure 7(a). As such, the data of δ_{τ_w} at '$\lambda_z^+ = \infty$' are not included in figure 7(a). It may be argued that the transverse travelling wave technique is pointless since the flapping motion of the actuators produces almost the same control performance. The DNS work by Du & Karniadakis (2000) and Du *et al.* (2002) may provide insight into the difference in the control performance between a transverse travelling wave and a real two-dimensional (2D) wave. Du *et al.*'s (2002) transverse travelling wave is induced by a spatial force close to the wall, given by $F_z = I\,e^{-y/\Delta}\,\sin((2\pi/\lambda_z)z - 2\pi f_o t)$, where I is the force magnitude and Δ the penetration depth. For $\lambda_z^+ \to \infty$, however, the 2D wave equation becomes $F_z = -I e^{-y/\Delta} \sin(2\pi f_o t)$, which is exactly the equation for a spanwise oscillatory force (Berger *et al.* 2000). Although spanwise oscillatory forcing corresponds to the 2D case of the transverse travelling wave, the drag reduction mechanisms differ between the two cases, and the near-wall flow structures are altered differently (Karniadakis & Choi 2003). Therefore, a transverse travelling wave does differ from a real 2D wave in terms of both the nature of the motion that is generated and the control outcome. We cannot therefore conclude from figure 7(a) that the 2D wave will always achieve the best performance that can be attained with the transverse travelling wave. Indeed, as shown in figure 7(b), δ_{τ_w} is not always smallest at $\varphi_{i,i+1} = 0$ (or '$\lambda_z^+ = \infty$'). Furthermore, through this investigation, we believe we can explain why increasing λ_z^+ may lead to a more pronounced drag reduction: with increasing λ_z^+ or reducing $\varphi_{i,i+1}$, the layer of generated streamwise vortices is more regularized, thus enhancing its effectiveness in acting as a barrier between the existing coherent structures and the wall as well as augmenting the turbulence dissipation rate. To our knowledge, this explanation was not provided in the previous numerical investigations (e.g. Du *et al.* 2002).

Given a limited maximum effective wavelength, a higher f_o^+ is desirable for drag reduction. Obviously, fluid may not respond quickly enough, due to its inertia, to the oscillation of actuators to form external streamwise vortices if f_o^+ exceeds a critical value, i.e. $f_{o,c}^+$. This proposition is corroborated by the fact that $f_{o,c}^+$ is coupled with A_o^+ (figure 6) and tends to decrease with increasing A_o^+, suggesting a limited maximum acceleration, which is given at the actuator tip by $(2\pi f_o^+)^2 A_o^+$. Further, the fluid mass involved in forming the streamwise vortices and its response to actuation depend on several parameters, such as the actuator length, its width and separation between actuators.

The layer of highly regularized streamwise vortices must be at the right distance from the wall or the right penetration depth to weaken or break most effectively the connection between the natural large-scale coherent structures and the wall and to reduce the friction drag, as in the case of spanwise wall oscillation (Jung *et al.* 1992; Choi *et al.* 1998), a spanwise oscillatory Lorentz force (Berger *et al.* 2000) or a transverse travelling force wave (Du & Karniadakis 2000; Du *et al.* 2002). When the

edge of the generated Stokes layer matches the location of the centre of near-wall streamwise vortices, interference to the turbulence production cycle is the greatest and thus the largest reduction in skin-friction drag is obtained. The oscillation amplitude A_o^+ directly influences the penetration depth Λ into the flow; the optimum $A_o^+ \approx 2.0$ produces $\Lambda^+ = 6\text{--}9$, which is comparable to the viscous-sublayer thickness. The centroids of natural near-wall large-scale streamwise vortices, with an averaged radius of approximately 15 wall units, are located, on average, at $y^+ \approx 20$ (Kim, Moin & Moser 1987), and the associated sweeps and ejections occur at an averaged distance $y^+ \approx 15$ (e.g. Wallace *et al.* 1972). In view of the likely jitter in location, most streamwise vortices may occur just above Λ^+. It may be inferred that the connection between the large-scale coherent structures and the wall is weakened most effectively, resulting in the maximum drag reduction, when the highly regularized streamwise vortices are introduced or the magnitude of Λ is below most of the coherent structures (figure 22).

The near-wall turbulence is maintained by a cycle located at $20 < y^+ < 60$, which can be self-sustained without any input from the core flow (Jiménez & Pinelli 1999). This cycle is closely associated with both near-wall streamwise vortices and the presence of low- and high-speed streaks. This self-sustained cycle may be interrupted once the near-wall streamwise vortices and velocity streaks are separated from the wall by the highly regularized streamwise vortices. The self-sustained process of near-wall turbulence may also be disrupted by near-wall spatial forces or wall-based actuations through either stabilizing the low-speed streaks or suppressing the high-speed streaks or breaking up the streamwise vortices (Karniadakis & Choi 2003; Kim 2003). Du & Karniadakis's (2000) and Du *et al.*'s (2002) transverse travelling wave decoupled the phase lock between streak formation and vortex generation (Karniadakis & Choi 2003), reducing the wall-normal fluctuating vorticity by nearly a factor of 2 and suppressing greatly the high-speed streaks near the wall. Based on their numerical data, Schoppa & Hussain (1998) proposed a control strategy for skin-friction drag reduction via bulk forcing using either counter-rotating vortex generators or colliding spanwise wall jets. The streamwise vortices near the wall were weakened as the instability of the low-speed streaks was impaired. They observed a 20 % drag reduction at a forcing magnitude of only 6 % of the channel centreline velocity. The wall-normal fluctuating vorticity was reduced by a factor of 2, compared with the uncontrolled flow. A spanwise-oscillating wall may also be used to attenuate significantly the self-sustained process by promoting a rapid decay of the streamwise vortices and thereby weakening the low-speed streaks (Dhanak & Si 1999).

6.6. *Scaling of drag reduction*

In this subsection, an empirical way of scaling the drag reduction is examined. The drag reduction δ_{τ_w} depends strongly on the control parameters A_o^+, f_o^+ and λ_z^+ (or $\varphi_{i,i+1}$). Consider the case when λ_z^+ reaches its maximum effective wavelength. Then, the functional relationship is reduced to $\delta_{\tau_w} = \delta_{\tau_w}(f_o^+, A_o^+)$. Figure 6(*a*,*b*) indicates clearly that f_o^+ and A_o^+ are closely coupled. One may surmise that δ_{τ_w} is connected to the energy input of the travelling wave, which is proportional to $(A_o^+ f_o^+)^2$. A careful analysis of the experimental data in figure 6(*a*,*b*), together with numerous trial-and-error attempts at least-squares-fitting the data, indicated that the relationship among δ_{τ_w}, f_o^+ and A_o^+ may be

$$\delta_{\tau_w} = f(A_o^+ f_o^+)\, \mathrm{e}^{-(A_o^+ - C)^2}, \tag{6.1}$$
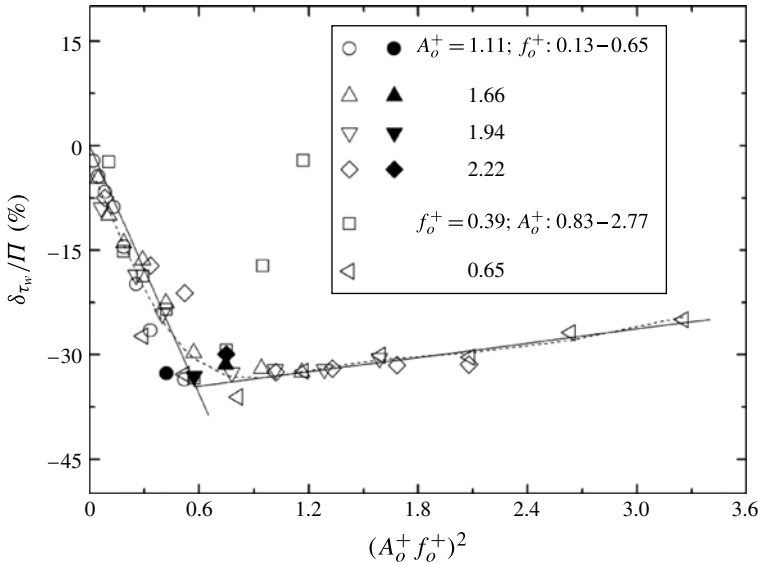
FIGURE 23. Dependence of δ_{τ_w}/Π on $(A_o^+ f_o^+)^2$ at $\lambda_z^+ \geqslant 250$. The two solid lines are linear fits to the data: $\delta_{\tau_w}/\Pi = -59.46(A_o^+ f_o^+)^2$ for $(A_o^+ f_o^+)^2 \leqslant 0.65$ and $\delta_{\tau_w}/\Pi = 3.41(A_o^+ f_o^+)^2 - 36.55$ for $(A_o^+ f_o^+)^2 > 0.65$. The dotted curve is $\delta_{\tau_w}/\Pi = a_1 e^{-[(A_o^+ f_o^+ - b_1)/c_1]^2} + a_2 e^{-[(A_o^+ f_o^+ - b_2)/c_2]^2}$, obtained by nonlinear fitting to the data, based on (6.3). The coefficients a_1, b_1, c_1, a_2, b_2 and c_2 are listed in table 3.

where $f(A_o^+ f_o^+)$ is a function of $A_o^+ f_o^+$ and C is constant. Equation (6.1) takes into account (i) a coupling between f_o^+ and A_o^+ and (ii) the Gaussian variation in δ_{τ_w} with A_o^+, shown in figure 6(*b*). The constant C is determined to be 2, i.e. the optimum oscillation amplitude $A_{o,opt}^+$ corresponding to the maximum δ_{τ_w}. In order to determine $f(A_o^+ f_o^+)$ in (6.1), we denote $e^{-(A_o^+ - 2)^2}$ by Π and plot δ_{τ_w}/Π against the input energy $(A_o^+ f_o^+)^2$. As shown in figure 23, we obtain a reasonably good collapse for almost all the data with either a linear least-squares fit by

$$\frac{\delta_{\tau_w}}{\Pi} = -59.46(A_o^+ f_o^+)^2, \quad (A_o^+ f_o^+)^2 \leqslant 0.65, \tag{6.2a}$$

and

$$\frac{\delta_{\tau_w}}{\Pi} = 3.41(A_o^+ f_o^+)^2 - 36.55, \quad (A_o^+ f_o^+)^2 > 0.65, \tag{6.2b}$$

or a nonlinear fit, *viz.*

$$\frac{\delta_{\tau_w}}{\Pi} = a_1 \exp\left[-\left(\frac{A_o^+ f_o^+ - b_1}{c_1}\right)^2\right] + a_2 \exp\left[-\left(\frac{A_o^+ f_o^+ - b_2}{c_2}\right)^2\right], \tag{6.3}$$

where the coefficients a_1, b_1, c_1, a_2, b_2 and c_2 are given in table 3.

Some interesting inferences can be made from (6.2) and (6.3). Firstly, writing (6.2*a*) as $\delta_{\tau_w} = -59.46\Pi(A_o^+ f_o^+)^2$, we see immediately that the factor (-59.46Π) or $-59.46\,e^{-(A_o^+ - 2)^2}$ can be understood to be the drag reduction for each unit energy input and is an indicator of the control efficiency. Secondly, δ_{τ_w}/Π declines approximately

a_1	b_1	c_1	a_2	b_2	c_2
-15.16	0.78	0.38	-28.95	1.45	0.88

TABLE 3. Coefficients of the proposed scaling factor ξ in (6.4).

linearly for $(A_o^+ f_o^+)^2 < 0.65$, suggesting that, given a small energy input, the control efficiency is almost linearly proportional to this energy. After reaching the minimum at $(A_o^+ f_o^+)^2 \approx 0.65$, δ_{τ_w}/Π rises very slowly, again almost linearly, as the input energy increases further, that is, when a threshold, in this case $(A_o^+ f_o^+)^2 \approx 0.65$, is exceeded, a further increase in the input energy affects the control efficiency adversely. Thirdly, the critical frequency $f_{o,c}^+$ for each specified A_o^+ may be predicted via (6.3). For a given A_o^+, we set $(\partial \delta_{\tau_w}/\partial f_o^+)|_{A_o^+} = 0$ to obtain $f_{o,c}^+$. This equation may be easily solved using a graphical method (Castillo 1988). The solutions for $f_{o,c}^+$ are 0.77, 0.52, 0.44 and 0.39 for $A_o^+ = 1.11$, 1.66, 1.94 and 2.22, respectively, very close to those observed from measurements, cf. figure 6(*a*) or the solid symbols in figure 23. In particular, specifying $A_o^+ = A_{o,opt}^+ = 2$ yields $f_{o,c}^+ = 0.43$, close to 0.4 as calculated by $\sqrt{0.65/A_{o,opt}^+{}^2}$. It is of interest to note that all the above values of A_o^+ and $f_{o,c}^+$ occur at $(A_o^+ f_o^+)^2 \approx 0.74$, close to the most efficient control $((A_o^+ f_o^+)^2, \delta_{\tau_w}/\Pi) \approx (0.65, -33\%)$ (figure 23). Alternatively, given f_o^+, we may predict $A_{o,opt}^+$ from (6.3). For example, with $f_o^+ = 0.4$, $A_{o,opt}^+ = 2.1$, corresponding to $((A_o^+ f_o^+)^2, \delta_{\tau_w}/\Pi) = (0.7, -32.3\%)$, again close to the most efficient control. Fourthly, for Berger *et al.*'s (2000) spanwise oscillatory Lorentz force and Du & Karniadakis's (2000) transverse travelling wave techniques, given a penetration depth Λ, the drag reduction scales with the energy input $I(f_o^+)^{-1}$ (Karniadakis & Choi 2003); similarly, given A_o^+ or Λ, the drag reduction scales with the energy input $(A_o^+ f_o^+)^2$ for the present technique. However, the unit force F_z/I imposed on the fluid is an exponential function of Λ, i.e. $F_z/I \sim e^{-y/\Lambda}$, whilst Π is given by $e^{-(A_o^+ - 2)^2}$. Fifthly, the maximum $\Pi = 1$ corresponds to $A_{o,opt}^+ = 2$, implying that the drag reduction for each unit energy input is largest and the control is most efficient when A_o^+ is optimal or the associated penetration depth is comparable to the viscous-sublayer thickness. Finally, two points $(f_o^+, A_o^+) = (0.39, 2.5)$ and $(0.39, 2.75)$, excluded when fitting (6.2), deviate significantly from the others. The value $f_o^+ = f_{o,c}^+ = 0.39$ is the critical frequency at $A_{o,opt}^+ \approx 2$. It seems that, at $f_o^+ = f_{o,c}^+$, δ_{τ_w}/Π cannot be described by (6.2) or (6.3) once A_o^+ or the penetration depth exceeds its optimum by an appreciable amount.

Figure 24 presents the dependence of δ_{τ_w} on a scaling factor ξ, defined by

$$\xi = -\frac{1}{36.1} \left\{ a_1 \exp\left[-\left(\frac{A_o^+ f_o^+ - b_1}{c_1}\right)^2 \right] + a_2 \exp\left[-\left(\frac{A_o^+ f_o^+ - b_2}{c_2}\right)^2 \right] \right\} \Pi. \quad (6.4)$$

Evidently, almost all the experimental data fall around a straight line, $\delta_{\tau_w} = -36.1\xi$, and δ_{τ_w} declines gradually with increasing ξ. Again, the two points $(f_o^+, A_o^+) = (0.39, 2.5)$ and $(0.39, 2.75)$ deviate significantly from this line. The scaling of drag reduction in figure 24 works for the maximum effective $\lambda_z^+ \geqslant 250$ (or $\varphi_{i,i+1} \leqslant 30°$).

6.7. *Drag reduction efficiency*

The effectiveness of the control technique can be evaluated through the control efficiency η, which may be defined by the ratio $\eta = P_{saved}/P_{used}$ (Berger *et al.* 2000),
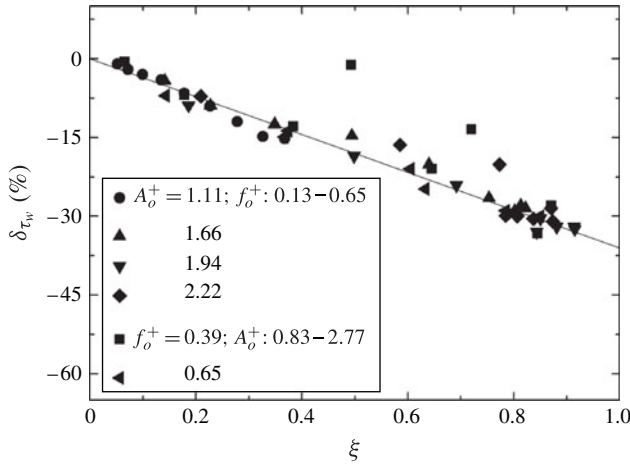
FIGURE 24. Dependence of δ_{τ_w} on the scaling factor ξ at $\lambda_z^+ \geqslant 250$. The solid line is a least-squares fit to the data, excluding two points $(f_o^+, A_o^+) = (0.39, 2.5)$ and $(0.39, 2.75)$.

where P_{saved} and P_{used} are the power saved and consumed, respectively. The power P_{saved} due to skin-friction drag reduction (δ_{τ_w}) can be calculated by multiplying δ_{τ_w} by the friction force and the free streamwise velocity, i.e. $P_{saved} = \delta_{\tau_w} \rho u_\tau^2 A_c U_\infty$, where A_c is the area over which δ_{τ_w} is obtained. Because δ_{τ_w} under a set of control parameters is dependent on x (figure 8), P_{saved} can then be rewritten as $P_{saved} = \rho u_\tau^2 U_\infty L_c \int_{x_o}^{x_c} \delta_{\tau_w} \, dx$, where L_c and $x_c - x_o$ are the spanwise and streamwise extents of the affected area downstream of the actuator array, respectively. Length L_c is taken to be the span of the entire actuator array, i.e. $L_c = 45$ mm or $L_c^+ = 312$. Subsequently, based on the results in figure 8, P_{saved} is estimated to be 6.41×10^{-6} W, with the optimum control parameters applied. On the other hand, the power P_{used} is due to the dissipation of the PZT actuators operated at an oscillation frequency f_o and driving voltage V_o, which can be calculated by $P_{used} = 6.28 N f_o C \tan(\delta) V_o^2$, where $C = 20$ nF and $\tan(\delta) = 1.7 \%$ are the capacitance and dissipation factor of the PZT material used, respectively, and $N = 16$ is the total number of actuator elements. Given $f_o = 300$ Hz and $V_o = 10$ V, we arrive at $P_{used} = 1.02 \times 10^{-3}$ W. Here, η is estimated to be 6.28×10^{-3}, which is of the same order as that when a spanwise oscillating Lorentz force (Berger *et al.* 2000) and wavy Lorentz force (Huang, Fan & Dong 2010) was used. Berger *et al.* (2000) ascribed the inefficiency of their control technique to the low conductivity of seawater and suggested that it was unlikely to obtain a net energy saving. At higher Reynolds number, as Jacobson & Reynolds (1998) discussed, the actuator size has to be reduced, decreasing its power consumption faster than the associated skin-friction drag because the power dissipation scales with the cantilever volume of the actuator but the skin-friction drag scales with the wall surface area. Du & Karniadakis (2000) and also Du *et al.* (2002) obtained an efficiency higher than unity in their drag reduction investigation based on a transverse travelling wave generated by discrete electromagnetic tiles. These tiles, covering less than 10 % of the total area, were actuated in a multiphase pulsing pattern. Their result suggests that a net energy saving is achievable in friction drag reduction investigations with discrete excitations on the wall. For the present investigation, extending longitudinally the actuation area, e.g. adding more rows of actuators, could slow down the recovery of the perturbed flow and substantially improve the control efficiency.

7. Conclusions

Active control of a fully developed TBL ($Re_\theta = 1000$) over a flat plate has been investigated with a view to reducing the skin-friction drag. The boundary layer is manipulated based on wall-normal oscillations generated by an array of 12–16 piezo-ceramic actuators flush-mounted to the wall surface. Driven by a sinusoidal voltage, each actuator oscillated independently and, by prescribing a phase shift between adjacent actuators, the wall-normal oscillation formed a discrete transverse travelling wave. A number of control parameters have been examined, including the wavelength ($\lambda_z^+ \geqslant 41.6$), amplitude ($A_o^+ = 0.83–2.77$) and frequency ($f_o^+ = 0.13–0.65$) of the oscillation. The friction drag was estimated from the streamwise mean-velocity profiles measured using a single hot wire in the viscous sublayer. Major conclusions are as follows.

(i) The transverse travelling wave formed by the wall-based discrete actuators generates, under the optimum control parameters ($A_o^+ \approx 2$, $f_o^+ \geqslant 0.39$ and $\lambda_z^+ \approx 250$ or $\varphi_{i,i+1} \approx 30°$), a layer of highly regularized streamwise vortices, which acts to weaken or even completely sever the connection between the large-scale coherent structures and the wall, thus interfering with the turbulence production cycle and resulting in significant drag reduction. The maximum drag reduction is 50 % at $x^+ = 17$. To our knowledge, this is the first time that this has been achieved with an array of discrete actuators. The skin-friction drag recovers rapidly downstream, returning to its uncontrolled level beyond $x^+ = 150$, due mainly to the very limited effective longitudinal extent of the actuation.

(ii) The effectiveness in breaking the connection between the large-scale coherent structures and the wall depends to a large extent on the strength of the introduced streamwise vortices, or how regular they are and how deeply they penetrate into the near-wall region. Oscillation amplitude $A_o^+ \approx 2$ produces the optimum penetration depth, i.e. $\Lambda^+ = 6–9$, which falls immediately below the location where the maximum rms value of ω_x occurs. Decreasing $\varphi_{i,i+1}$ or increasing λ_z^+ enhances the spanwise regularization of these introduced streamwise vortices and increases the wave speed w_t^+. Therefore, these vortices may act more effectively to weaken the connection between the large-scale coherent structures and the wall, resulting in the monotonic decrease in δ_{τ_w} with increasing λ_z^+ (< 250). Owing to the discrete nature of the actuator array, the effective wavelength is not increased at all for any increase in λ_z^+ beyond a certain level, resulting in the 'saturation' of δ_{τ_w} at $\lambda_z^+ \approx 250$, which is the maximum effective wavelength for the present experimental conditions. Since $w_t^+ = \lambda_z^+ f_o^+$, a higher f_o^+ is desirable for drag reduction. On the other hand, owing to its inertia, the fluid may not be able to respond quickly enough to actuation to form streamwise vortices if f_o^+ exceeds a critical value, $f_{o,c}^+$, which is coupled to A_o^+ (figure 6).

(iii) Several changes to the flow structure occur under control. The linear region of the $\overline{U}^+$ profile or the viscous-sublayer thickness grows by approximately 100 %, compared to the natural case. As such, the log-law region is displaced upwards. The frequency, intensity and duration of bursts are all reduced, by more than 20 % at $y^+ = 6.5$. The spectral analysis, the distributions of streaky structures, the characteristics of u and $\partial u/\partial t$, and the magnitude of the Taylor microscale all point to less energetic large-scale coherent structures and weakened high-momentum sweep motions. The energy dissipation rate, as inferred from the variance of $\partial u/\partial t$, is increased in the near-wall region, thus contributing to the significant drag reduction.

(iv) A scaling for the drag reduction is proposed based on the present experimental parametric study. Given an adequately large wavelength of the travelling wave, the scaling works reasonably well, except at $f_o^+ = f_{o,c}^+$ and $A_o^+ > A_{o,opt}^+$. The drag reduction per unit energy input, an indicator of control efficiency, is found to scale with the energy input of the control; it increases almost linearly with the energy input until it reaches a threshold energy input and then decreases linearly and slowly.

Active control of a TBL for skin-friction drag reduction represents a fascinating challenge to the experimental fluid dynamics community (e.g. Kasagi *et al.* 2009). Despite achieving a large drag reduction, the present control efficiency is very low, owing to the rapid recovery of the reduced wall shear stress. Deploying more rows of the actuator array at several x locations may be one way of slowing down the recovery, thus improving the control efficiency. A closed-loop control is currently being developed to improve the control efficiency as well as, hopefully, our understanding of the flow physics and control mechanisms.

REFERENCES

ALFREDSSON, P. H. & JOHANSSON, A. V. 1984 On the detection of turbulence-generating events. *J. Fluid Mech.* **139**, 325–345.

ANTONIA, R. A. & BISSET, D. K. 1990 Spanwise structure in the near-wall region of a turbulent boundary layer. *J. Fluid Mech.* **210**, 437–458.

ANTONIA, R. A., FULACHIER, L., KRISHNAMOORTHY, L. V., BENABID, T. & ANSELMET, F. 1988 Influence of wall suction on the organized motion in a turbulent boundary layer. *J. Fluid Mech.* **190**, 217–240.

ANTONIA, R. A. & KIM, J. 1991 Turbulent Prandtl number in the near-wall region of a turbulent channel flow. *Intl J. Heat Mass Transfer* **34** (7), 1905–1908.

ANTONIA, R. A., ZHU, Y. & SOKOLOV, M. 1995 Effect of concentrated wall suction on a turbulent boundary layer. *Phys. Fluids* **7**, 2465–2474.

BERGER, T. W., KIM, J., LEE, C. & LIM, J. 2000 Turbulent boundary layer control utilizing the Lorentz force. *Phys. Fluids* **12**, 31–49.

BERNARD, P. S., THOMAS, J. M. & HANDLER, R. A. 1993 Vortex dynamics and the production of Reynolds stress. *J. Fluid Mech.* **253**, 385–419.

BLACKWELDER, R. F. & HARITONIDIS, J. H. 1983 Scaling of the bursting frequency in turbulent layers. *J. Fluid Mech.* **132**, 87–103.

BLACKWELDER, R. F. & KAPLAN, R. E. 1976 On the wall structure of the turbulent boundary layer. *J. Fluid Mech.* **76**, 89–112.

CASTILLO, E. 1988 *Extreme Value Theory in Engineering.* Academic Press.

CHEN, C.-H. P. & BLACKWELDER, R. F. 1978 Large-scale motion in a turbulent boundary layer: a study using temperature contamination. *J. Fluid Mech.* **89**, 1–31.

CHOI, H., MOIN, P. & KIM, J. 1993 Direct numerical simulation of turbulent flow over riblets. *J. Fluid Mech.* **255**, 503–539.

CHOI, K.-S. 1989 Near-wall structure of a turbulent boundary layer with riblets. *J. Fluid Mech.* **208**, 417–458.

CHOI, K.-S. 2002 Near-wall structure of turbulent boundary layer with spanwise-wall oscillation. *Phys. Fluids* **14** (7), 2530–2542.

CHOI, K.-S. & CLAYTON, B. 2001 The mechanism of turbulent drag reduction with wall oscillation. *Intl J. Heat Fluid Flow* **22**, 1–9.

CHOI, K.-S., DEBISSCHOP, J.-R. & CLAYTON, B. R. 1998 Turbulent boundary-layer control by means of spanwise-wall oscillation. *AIAA J.* **36** (7), 1157–1163.

DEPARDON, S., LASSERRE, J. J., BOUEILH, L. E. & BORÉE, J. 2005 Skin friction pattern analysis using near-wall PIV. *Exp. Fluids* **39**, 805–818.

DHANAK, M. R. & SI, C. 1999 On reduction of turbulent wall friction through spanwise wall oscillations. *J. Fluid Mech.* **383**, 175–195.

DI CICCA, G. M., IUSO, G., SPAZZINI, P. G. & ONORATO, M. 2002 Particle image velocimetry investigation of a turbulent boundary layer manipulated by spanwise wall oscillations. *J. Fluid Mech.* **467**, 41–56.

DU, Y. & KARNIADAKIS, G. E. 2000 Suppressing wall turbulence by means of a transverse travelling wave. *Science* **288**, 1230–1234.

DU, Y., SYMEONIDIS, V. & KARNIADAKIS, G. E. 2002 Drag reduction in wall-bounded turbulence via a transverse travelling wave. *J. Fluid Mech.* **457**, 1–34.

ENDO, T., KASAGI, N. & SUZUKI, Y. 2000 Feedback control of wall turbulence with wall deformation. *Intl J. Heat Fluid Flow* **21**, 568–575.

GAD-EL-HAK, M. 2000 *Flow Control: Passive, Active, and Reactive Flow Management*. Cambridge University Press.

GROSJEAN, C., LEE, G. B., HONG, W., TAI, Y. C. & HO, C. M. 1998 Micro balloon actuators for aerodynamic control. In *Proceedings of the 11th MEMS Workshop, Heidelberg, 25–29 January 1998*, pp. 166–171. IEEE.

HUANG, J. F., ZHOU, Y. & ZHOU, T. 2006 Three-dimensional wake structure measurement using a modified PIV technique. *Exp. Fluids* **40**, 884–896.

HUANG, L., FAN, B. & DONG, G. 2010 Turbulent drag reduction via a transverse wave travelling along streamwise direction induced by Lorentz force. *Phys. Fluids* **22**, 015103.

HUTCHINS, N. & CHOI, K.-S. 2002 Accurate measurements of local skin friction coefficient using hot-wire anemometry. *Prog. Aeronaut. Sci.* **38**, 421–446.

ITOH, M., TAMANO, S., YOKOTA, K. & TANIGUCHI, S. 2006 Drag reduction in a turbulent boundary layer on a flexible sheet undergoing a spanwise travelling wave motion. *J. Turbul.* **7** (27), 1–17.

IUSO, G., DI CICCA, G. M., ONORATO, M., SPAZZINI, P. G. & MALVANO, R. 2003 Velocity streak structure modifications induced by flow manipulation. *Phys. Fluids* **15**, 2602–2612.

IUSO, G., ONORATO, M., SPAZZINI, P. G. & DI CICCA, G. M. 2002 Wall turbulence manipulated by large-scale streamwise vortices. *J. Fluid Mech.* **473**, 23–58.

JACOBSON, S. A. & REYNOLDS, W. C. 1998 Active control of streamwise vortices and streaks in boundary layers. *J. Fluid Mech.* **360**, 179–211.

JIMÉNEZ, J. & PINELLI, A. 1999 The autonomous cycle of near-wall turbulence. *J. Fluid Mech.* **389**, 335–359.

JOHANSSON, A. V., ALFREDSSON, P. H. & KIM, J. 1991 Evolution and dynamics of shear-layer structures in near-wall turbulence. *J. Fluid Mech.* **224**, 579–599.

JUNG, W. J., MANGIAVACCHI, N. & AKHAVAN, R. 1992 Suppression of turbulence in wall-bounded flows by high-frequency spanwise oscillations. *Phys. Fluids* A **4** (8), 1605–1607.

KANG, S. & CHOI, H. 2000 Active wall motions for skin-friction drag reduction. *Phys. Fluids* **12** (12), 3301–3304.

KARNIADAKIS, G. E. & CHOI, K.-S. 2003 Mechanisms on transverse motions in turbulent wall flows. *Annu. Rev. Fluid Mech.* **35**, 45–62.

KASAGI, N., SUZUKI, Y. & FUKAGATA, K. 2009 Microelectromechanical systems-based feedback control of turbulence for skin friction reduction. *Annu. Rev. Fluid Mech.* **41**, 231–251.

KHOO, B. C., CHEW, Y. T. & TEO, C. J. 2000 On near-wall hot-wire measurements. *Exp. Fluids* **29**, 448–460.

KIM, J. 1983 On the structure of wall-bounded turbulent flows. *Phys. Fluids* **26** (8), 2088–2097.

KIM, J. 2003 Control of turbulent boundary layers. *Phys. Fluids* A **15**, 1093–1105.

KIM, J. 2011 Physics and control of wall turbulence for drag reduction. *Phil. Trans. R. Soc.* A **369**, 1396–1411.

KIM, J., MOIN, P. & MOSER, R. 1987 Turbulence statistics in fully developed channel flow at low Reynolds number. *J. Fluid Mech.* **177**, 133–166.

KLINE, S. J., REYNOLDS, W. C., SCHRAUB, F. A. & RUNSTADLER, P. W. 1967 The structure of turbulent boundary layers. *J. Fluid Mech.* **30**, 741–773.

KRAVCHENKO, A. G., CHOI, H. & MOIN, P. 1993 On the generation of near-wall streamwise vortices to wall skin friction in turbulent boundary layers. *Phys. Fluids* A **5**, 3307–3309.

LAADHARI, F., SKANDAJI, L. & MOREL, R. 1994 Turbulence reduction in a boundary layer by a local spanwise oscillating surface. *Phys. Fluids* **6** (10), 3218–3220.

LIEPMANN, H. W. & NARASIMHA, R. (Eds) 1988 *Turbulence Management and Relaminarisation*. Springer.

LU, S. S. & WILLMARTH, W. W. 1973 Measurements of the structure of the Reynolds stress in a turbulent boundary layer. *J. Fluid Mech.* **60**, 481–511.

MARQUILLIE, M., EHRENSTEIN, U. & LAVAL, J.-P. 2011 Instability of streaks in wall turbulence with adverse pressure gradient. *J. Fluid Mech.* **681**, 205–240.

METZGER, M. 2006 Length and time scales of the near-surface axial velocity in a high Reynolds number turbulent boundary layer. *Intl J. Heat Fluid Flow* **27**, 534–541.

NAGANO, Y., TSUJI, T. & HOURA, T. 1998 Structure of turbulent boundary layer subjected to adverse pressure gradient. *Intl J. Heat Fluid Flow* **19**, 563–572.

ONORATO, M. & IUSO, G. 2001 Probability density function and 'plus' and 'minus' structure functions in a turbulent channel flow. *Phys. Rev.* E **63**, 025203(R).

ORLANDI, P. & JIMÉNEZ, J. 1994 On the generation of turbulent wall friction. *Phys. Fluids* A **6**, 634–641.

PANG, J. & CHOI, K.-S. 2004 Turbulent drag reduction by Lorentz force oscillation. *Phys. Fluids* **16** (5), L35–L38.

PARK, Y.-S., PARK, S.-H. & SUNG, H. J. 2003 Measurement of local forcing on a turbulent boundary layer using PIV. *Exp. Fluids* **34**, 697–707.

QUADRIO, M. & RICCO, P. 2004 Critical assessment of turbulent drag reduction through spanwise wall oscillations. *J. Fluid Mech.* **521**, 251–271.

RATHNASINGHAM, R. & BREUER, K. S. 2003 Active control of turbulent boundary layers. *J. Fluid Mech.* **495**, 209–233.

REBBECK, H. & CHOI, K.-S. 2006 A wind-tunnel experiment on real-time opposition control of turbulence. *Phys. Fluids* **18**, 035103.

ROBINSON, S. K. 1991 Coherent motions in the turbulent boundary layer. *Annu. Rev. Fluid Mech.* **23**, 601–639.

SANDBORN, V. A. & LIU, C. Y. 1968 On turbulent boundary-layer separation: part 2. *J. Fluid Mech.* **32**, 293–304.

SCHLICHTING, H. & GERSTEN, K. 2000 *Boundary-Layer Theory*. Springer.

SCHOPPA, W. & HUSSAIN, F. 1998 A large-scale control strategy for drag reduction in turbulent boundary layer. *Phys. Fluids* **10** (5), 1049–1051.

SCHOPPA, W. & HUSSAIN, F. 2002 Coherent structure generation in near-wall turbulence. *J. Fluid Mech.* **453**, 57–108.

SEGAWA, T., KAWAGUCHI, Y., KIKUSHIMA, Y. & YOSHIDA, H. 2002 Active control of streak structures in wall turbulence using an actuator array producing inclined wavy disturbances. *J. Turbul.* **3**, 1–15.

SIMPSON, R. L., CHEW, Y.-T. & SHIVAPRASAD, B. G. 1981 The structure of a separating turbulent boundary layer. Part 1. Mean flow and Reynolds stresses. *J. Fluid Mech.* **113**, 23–51.

SIMPSON, R. L., STRICKLAND, J. H. & BARR, P. W. 1977 Features of a separating turbulent boundary layer in the vicinity of separation. *J. Fluid Mech.* **79**, 553–594.

TARDU, S. F. 2001 Active control of near-wall turbulence by local oscillating blowing. *J. Fluid Mech.* **439**, 217–253.

TARDU, S. F. & DOCHE, O. 2009 Active control of the turbulent drag by a localized periodical blowing dissymmetric in time. *Exp. Fluids* **47**, 19–26.

VAUGHAN, N. J. & ZAKI, T. A. 2011 Stability of zero-pressure-gradient boundary layer distorted by unsteady Klebanoff streaks. *J. Fluid Mech.* **681**, 116–153.

WALLACE, J. M., ECKELMANN, H. & BRODKEY, R. S. 1972 The wall region in turbulent shear flow. *J. Fluid Mech.* **54**, 39–48.

WASH, M. J. 1983 Riblets as a viscous drag reduction technique. *AIAA J.* **21**, 485–486.

WILKINSON, S. P. & BALASUBRAMANIAN, R. 1985 Turbulent burst control through phase-locked traveling surface depressions. *AIAA Paper* 85-0536.